



Critical Heat Flux of Confined Round Single Jet and Jet Array Impingement Boiling

V.S. Devahdhanush, Issam Mudawar*

Boiling and Two-Phase Flow Laboratory (PU-BTFL), School of Mechanical Engineering, Purdue University, 585 Purdue Mall, West Lafayette, IN 47907, USA

ARTICLE INFO

Article history:

Received 25 September 2020

Revised 17 December 2020

Accepted 19 December 2020

Available online 19 January 2021

Keywords:

jet impingement
confined jets
two-phase flow
boiling
critical heat flux
design correlation

ABSTRACT

This study involves experimental investigation of key parameters influencing CHF for confined round single jets and jet arrays impinging normally onto square heated surfaces. The experiments are performed using R-134a, a fluid widely used for thermal management of electronic and power devices, especially in aerospace applications. A comprehensive R-134a CHF database is acquired that considers the effects of various geometrical parameters and operating conditions. Close examination of the data trends reveals several strategies to augment CHF, such as increasing jet velocity and/or total mass flow rate and employing larger jet diameters for a fixed velocity or smaller diameters for a fixed flow rate. Higher CHF is also achieved by increasing saturation pressure for a fixed inlet fluid temperature (i.e., higher saturation pressures combined with higher inlet subcooling). Fluid exit qualities point to two different CHF mechanisms: subcooled CHF at high flow rates and saturated CHF at low flow rates. Underlying mechanisms are also propounded for two types of CHF transients: a sudden sharp temperature escalation at lower flow rates and a mild gradual increase at higher flow rates. Close inspection of the heating surface following CHF tests shows localized burnout patterns which provide significant insight into both the flow characteristics within the confinement region and the spatial distribution of surface temperature resulting from jet interactions. Statistical inference techniques are used in conjunction with the new understanding of fluid flow and heat transfer physics to formulate a new correlation form for CHF. The resulting correlation, which is based on a consolidated database of the present R-134a and previous FC-72 data, shows good prediction accuracy, evidenced by a mean absolute error of 16.66% for both fluids and over broad ranges of geometrical parameters and operating conditions.

© 2020 Elsevier Ltd. All rights reserved.

1. Introduction

1.1. Two-phase Thermal Management of High Heat Flux Electronic and Power Devices

Operation of many modern devices requires dissipating finite amounts of heat. Thermal management of these components is vital to ensure both reliable and safe operation. This is especially true in the case of electronic and power devices, which, for several decades, have been undergoing simultaneous miniaturization in size and increase in power dissipation, the net effects of which has been a rapid escalation in heat dissipation per unit volume and per unit device surface area. For example, heat dissipation from computer chips exceeded 100 W/cm^2 as early as the mid-1980s [1], and recent device developments, especially in aerospace and

defense applications, point to the need to tackle dissipative heat fluxes in excess of 1000 W/cm^2 [2].

It is now widely acknowledged that conventional thermal management methods like air convection (using both surface enhancement and fans) and single-phase liquid cooling schemes are simply no longer capable of tackling cooling needs for high-performance devices. This has caused thermal engineers to pursue a variety of phase change schemes, which ameliorate cooling performance by capitalizing on the cooling fluid's latent heat of vaporization in addition to sensible heat. The development of two-phase cooling concepts and design tools has been a primary objective of investigations at the Purdue University Boiling and Two-Phase Flow Laboratory (PU-BTFL) dating back to 1984. These include capillary devices [3], pool boiling thermosyphons [4–6], falling films [7,8], macro-channel flow boiling [9–11], micro-channel flow boiling [2,12–14], spray cooling [15], and jet impingement cooling [16].

A comprehensive review [17] of two-phase cooling solutions points to three best cooling candidates for thermal management solutions for very high heat flux applications: mini-/micro-channel

* Corresponding author. URL: <https://engineering.purdue.edu/BTFL>
E-mail address: mudawar@ecn.purdue.edu (I. Mudawar).

Nomenclature

A	area
A_r	ratio of total nozzle area to heated surface area, $A_r = NA_n/A_s$
Ar	Archimedes number
C	empirical coefficient
c_p	specific heat at constant pressure
D	diameter
Fr	Froude number
G	mass velocity
g	gravitational acceleration
H	jet height (= height of confinement channel)
h	enthalpy
h_{fg}	latent heat of vaporization
Ja^*	modified Jakob number, $Ja^* = c_{p,f} \Delta T_{sub,in} / h_{fg}$
k	thermal conductivity
L	length
\dot{m}	total mass flow rate
N	number of jets
n	number of datapoints; number of test cases
P	pressure
Q_v	volumetric flow rate
q''	heat flux
q''_{CHF}	critical heat flux
q''_{CHF}^*	dimensionless critical heat flux, $q''_{CHF}^* = q''_{CHF} / (\rho_g h_{fg} U_n)$
Re	Reynolds number
T	temperature
ΔT_{sat}	surface superheat, $\Delta T_{sat} = T_s - T_{sat}$
ΔT_{sub}	fluid subcooling, $\Delta T_{sub} = T_{sat} - T_f$
t	time
U_n	velocity of jet at nozzle exit
W_n	nozzle width in slot jet studies
We	Weber number
x_e	thermodynamic equilibrium quality

Greek symbols

ε	effectiveness
θ	percentage predicted within $\pm 30\%$
λ_c	capillary length, $\lambda_c = \sqrt{\sigma / g(\rho_f - \rho_g)}$
μ	dynamic viscosity
ξ	percentage predicted within $\pm 50\%$
ρ	density
σ	surface tension

Subscripts

c	unit jet cell
$char$	characteristic with respect to nozzle diameter
$crit$	critical
exp	experimental
f	liquid
g	vapor
h	heated
in	inlet
n	jet nozzle exit; each nozzle
out	outlet
$pool$	pool boiling
$pred$	predicted
s	surface; solid
sat	saturation
SS	steady state
sub	subcooling
tc	thermocouple

z	local
-----	-------

Acronyms

CHF	Critical Heat Flux
MAE	Mean Absolute Error (%)
ONB	Onset of Nucleate Boiling
ONBD	Onset of Nucleate Boiling Degradation
RMSE	Root Mean Square Error (%)

heat sinks, spray cooling, and jet impingement cooling. While the three provide competing performance merits, each also suffers disadvantages stemming from either performance concerns or lack of technical knowhow. For example, mini-/micro-channel heat sinks are prone to high pressure drop, two-phase flow instabilities, and large temperature gradients in the direction of coolant flow. Application of spray cooling is highly complicated by dependence of cooling performance on an unusually large number of parameters, rendering it often less favorable than mini-/micro-channel heat sinks or jet impingement cooling. Lastly, a key drawback of jet impingement is high coolant flow rate, which is necessitated by a need to use multiple jet arrays to maintain surface temperature uniformity. The present study is concerned entirely with jet impingement cooling.

1.2. Two-Phase Jet Impingement Cooling

Jet impingement typically involves transfer of a high-velocity fluid onto a heated surface. The fluid jet usually strikes the hot surface perpendicularly, but researchers have also investigated oblique/inclined jets where the jet strikes the surface at other angles [18]. The earliest works on jet impingement focused on use of gases such as air [19], but attention later shifted to using liquids in pursuit of improved cooling rates. To cater to very high heat flux applications, researchers started taking advantage of phase change with liquid jets [20]. Jet impingement with boiling has applications in both heat-flux-controlled and temperature-controlled cooling systems. Modern examples of the former are shown in Fig. 1 while the latter include metal alloy heat treating, rolling, casting, and extrusion.

Some of the advantages of jet impingement compared to the other high performance cooling schemes are (i) comparatively lower pressure drop for equal heat flux removal, (ii) ability to cool large surface areas by using multiple jet arrays, (iii) cooling complex system shapes and multiple devices using the same cooling system, (iv) improved surface temperature uniformity (by using multiple jet arrays), and (v) suitability for both microgravity and high-body-force environments [21,22] which stems from reliance on high flow inertia. But jet impingement is not without shortcomings. They include (i) need for high-flow-rate pumping systems, and (ii) potential adverse effects to heated surface or device caused by both high impact and frictional shear stresses.

Jet impingement can be broadly classified into three categories: free-surface [20], submerged [23], and confined [22]. A free-surface jet is one where the liquid strikes the heated surface amidst a gaseous medium or vapor. Submerged jets have the jet nozzle under a pool of liquid, but the free surface of the liquid can still be exposed to a gas or vapor. With confined jets, the jet fluid issued from the nozzle is forced to flow in a narrow confinement space separating the nozzle orifice from the heating surface. Among the three categories, confined jets provide the best heat transfer performance, especially in high heat flux situations, where boiling occurs within the confinement space. Without the confinement, boiling in the wall liquid flow emanating from the impingement zone causes it to shatter and splash away from the heating surface. Confinement greatly reduces the liquid splashing, forcing more liquid

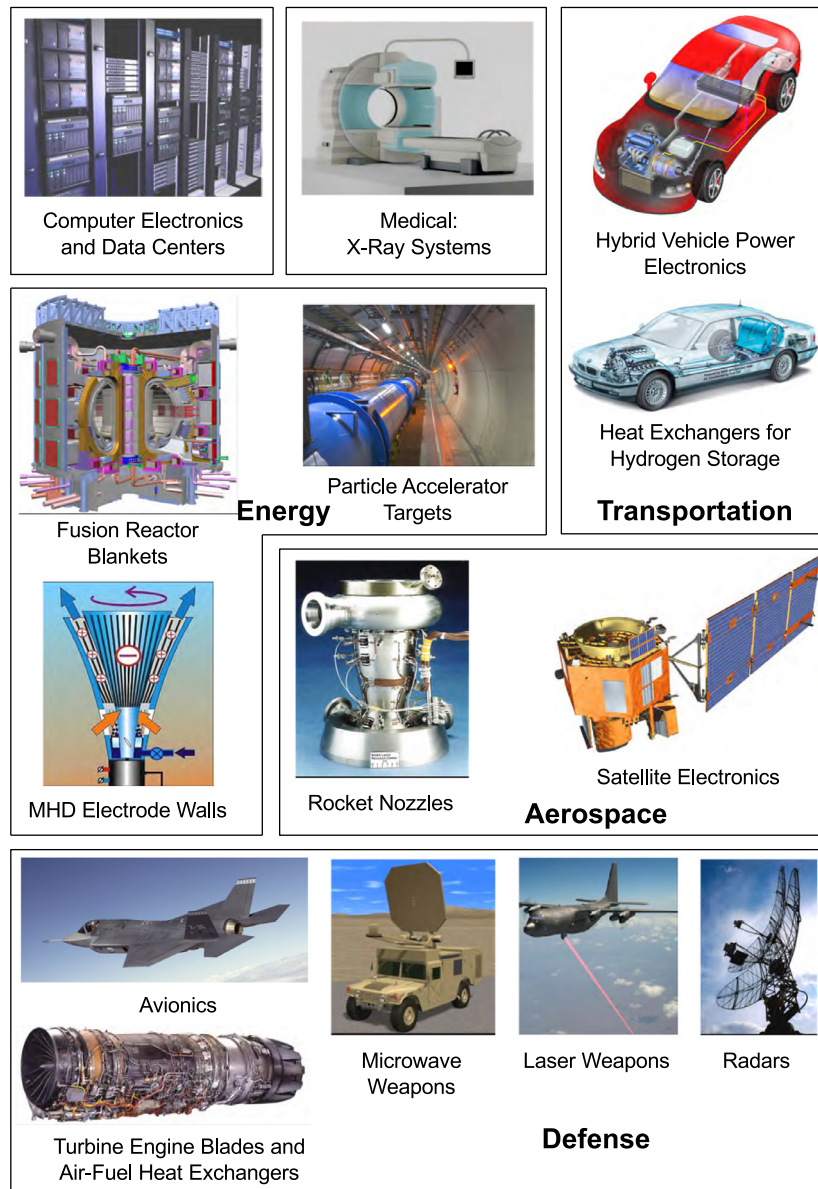


Fig. 1. Examples of applications demanding high heat flux cooling solutions. Adapted from Mudawar [17].

contact with the surface, thereby reducing the possibility of premature surface dryout [24–27]. Another merit of the splash prevention, especially when using dielectric fluid to cool an exposed electronic or power device, is resisting contamination with non-condensable gases which are known to greatly compromise heat transfer performance during boiling [28]. Yet another advantage is preventing the spent hot fluid from recirculating back towards the heating surface where it might compromise cooling performance [21].

1.3. Critical Heat Flux (CHF) for Impinging Jets

Critical Heat Flux (CHF) is arguably the most important safety and design parameter for any application involving phase change cooling of heat-flux controlled surfaces. Its occurrence is commonly traced with the aid of a boiling curve, a plot of surface heat flux versus surface-to-fluid temperature. A boiling curve reflects the drastic changes in boiling regimes and therefore cooling performance occurring with increasing heat flux. For most modern high-heat-flux applications, the regime of primary interest is nu-

cleate boiling, which offers the advantages of most superior heat transfer performance and lowest surface temperatures. CHF is the upper heat flux limit for nucleate boiling, exceeding which would cause the surface temperature to escalate uncontrollably, often to levels triggering permanent damage to the device being cooled. Optimum cooling is therefore achieved by maintaining cooling performance (i) well within the nucleate boiling regime but (ii) safely below CHF. Accurate determining of CHF therefore represents the most paramount starting point when designing a two-phase thermal management system.

Katto and Kunihiro [20] published the first systematic study explaining the mechanism of CHF for both free and submerged impinging jets. They employed a gravity-driven round jet of water which impinged normally on a circular heated surface. They observed boiling in the radial wall liquid layer emanating from the impingement zone causing splashing of liquid away from the surface, which was a primary precursor for CHF occurrence. They attributed the splashing to appreciable normal momentum of vapor produced at the surface. The intense vapor production both inhib-

ited access of fresh liquid to the heated surface and promoted formation of dry patches along the surface, both clear signs of ensuing burnout. Increasing jet velocity was found to increase CHF by more effectively piercing coalescent vapor masses on the surface. Their study was followed by several others on jet impingement CHF performed using different fluids, geometries, and operating conditions.

One of the first correlations for jet impingement CHF was proposed by Monde and Katto [24] for single free-surface round jets of water and R-113 impinging on both upward- and downward-facing circular heated surfaces of diameter D_s and presented as

$$\frac{q''_{CHF}}{\rho_g h_{fg} U_n} = 0.0745 \left(\frac{\rho_f}{\rho_g} \right)^{0.725} \left(\frac{\sigma}{\rho_f U_n^2 D_s} \right)^{1/3} (1 + \varepsilon_{sub}), \quad (1a)$$

where ε_{sub} is the subcooling effectiveness, defined as

$$\varepsilon_{sub} = 2.7 \left(\frac{\rho_f}{\rho_g} \right)^{0.5} \left(\frac{c_{p,f}(T_{sat} - T_{in})}{h_{fg}} \right)^2. \quad (1b)$$

Their experiments showed CHF was a strong function of the jet nozzle velocity but unaffected by jet diameter, which implies that, unlike other cooling schemes (e.g., channel flow boiling), CHF is not dictated by coolant flow rate. They also observed a monotonic increase in CHF with increasing subcooling. They formulated their correlation for dimensionless CHF, $q''_{CHF} = q''_{CHF} / (\rho_g h_{fg} U_n)$, as a function of Weber number, liquid-to-vapor density ratio, and a subcooling function of both density ratio and Jacob number. The correlation suggested a strong influence of surface tension on CHF, as with pool boiling, and the density ratio term facilitated correlation of data for the two fluids and different operating conditions.

Over the course of several decades, most researchers employed essentially the same dimensionless formulation of Monde and Katto to correlate their CHF data. For example, Katto and Ishii [29] used the same form for CHF data for single free-surface planar jets of saturated water, R-113, and trichloroethane impinging on a downward-facing rectangular surface, but with slight variations in dimensionless parameters because of the different jet shape; they also employed different empirical constants. Among other studies employing the same formulation, Katto and Shimizu [25] conducted experiments with free-surface circular jets of R-12 at various pressures, and water and R-113 at atmospheric pressure, and observed the presence of two main CHF regimes: V- and I-regimes. The V-regime was characterized by a CHF dependence on jet velocity while the I-regime was independent of velocity. The V- and I-regimes were prevalent at lower and higher jet velocities, respectively, and the point of transition between the two shifted towards lower velocities at higher pressures. They also observed two additional minor regimes: D-regime corresponding to jet velocities that were too small to induce splashing (which was also observed in Katto and Kunihiro's [20] experiments), and HP-regime specific to very high pressures. They also proposed various criteria to demarcate between the different regimes. Soon, many studies were published by the same research group that culminated in new CHF predictive tools, such as those for submerged wall jets [30], free-surface round jets (incorporating effects of heated surface area) [31], plane wall jets (with CHF predicted using a hydrodynamic model) [32], free-surface round jets in the V-regime (also using hydrodynamic model) [33], free-surface round jets in the L-regime (characterized by a combination of very small jet velocities and large surface-to-nozzle diameter ratio) [34]; they also developed a generalized correlation for all CHF regimes based on data collected over many years [26]. Another generalized correlation was proposed by Katto and Yokoya [35] for single circular jets impinging on circular surfaces based on prior data for water, R-113, and R-12. The form of this correlation is significantly different from those proposed earlier.

Monde *et al.* [36] was the first to study the effects of multiple jets on CHF, using two to four free-surface round jets of water and R-113 impinging onto a circular heated surface at various locations. They proposed a correlation with different empirical constants for burnout happening at the jet center and the surface edges. Noticing that their correlation had a form similar to that of Monde's single-jet correlation [31], they suggested strong similarity in burnout mechanism between single and multiple jets. In parallel, Sharan and Lienhard [37] re-correlated the data of Monde [26] based on a mechanical energy stability criterion. Nonn *et al.* [38] proposed yet another correlation for free-surface circular jets of dielectric fluid FC-72.

The first correlations for confined jets were proposed by Mudawar and Wadsworth [39], and McGillis and Carey [40] for slot jets of FC-72 and circular jets of R-113, respectively. Using an array of confined jets instead of a single jet has shown improved heat transfer performance and augmented CHF for the same flow rate. Numerous correlations have been proposed based on data for confined jet arrays [22,41–43]. To achieve highly compact packaging of the jet hardware, Meyer *et al.* [21] proposed using confined re-entrant planar jets, where a single jet plate was used to both issue the jets and tackle return of the spent fluid.

For several decades, all jet-impingement CHF correlations were constructed by numerically fitting experimental data to physically determined functional forms. In 2011, Cong *et al.* [44] employed artificial neural network and genetic algorithm principles to correlate a database collected from the literature, and showed their model yielded the lowest prediction errors. Another significantly different predictive method was proposed by Cardenas and Narayanan [45], who employed a forced convection CHF model for both free-surface and submerged jets. Grassi and Testi [46] recently proposed yet another predictive method for both submerged and electrohydrodynamic jets based on liquid-vapor interfacial instability theory. Both Cardenas and Narayanan's and Grassi and Testi's CHF relations were presented as ratios of jet impingement CHF to pool boiling CHF, which required a separate correlation for the latter to determine the jet CHF values.

Apart from the above-mentioned predictive methods, many other correlations have been proposed based on few datapoints and narrow ranges of operating conditions [47–51].

1.4. Objectives of the Study

It is clear that confined arrays of circular jets provide superior two-phase cooling performance, especially CHF, compared to free-surface arrays and both free-surface and confined single jets. This motivated use of the confined array configuration as a highly effective, very compact, and practical thermal management scheme for removal of very high heat fluxes from electronic and power devices found in many modern applications. While several of the studies presented in the previous section explored development of correlations suitable to several coolant types, limited use of water for these applications and very large differences in thermophysical properties between water on one hand and both refrigerants and fluorochemicals on the other hand meant aiming to develop broad-ranged correlations that include all three coolant types might in fact compromise the accuracy of predictions for refrigerants and fluorochemicals, which are the coolants most commonly used in applications of interest. Therefore, the present study is focused on performance of these two specific fluid types, albeit with an effort to include broad ranges of jet array geometrical configurations and operating conditions.

The representative fluids used in the present study to develop a predictive CHF correlation for confined arrays of circular jets are refrigerant R-134a and dielectric coolant FC-72. While the latter fluid has been used in a variety of direct-immersion electronic

cooling situations, R-134a is a refrigerant widely used in thermal management systems, especially in the aerospace industry, and for which jet impingement information is quite sparse.

In the present study, an experimental investigation is conducted to explore dependence of CHF for R-134a confined round jet arrays on key geometrical parameters and broad ranges of operating conditions. Aside from the CHF measurements, close inspection of the heating surface following CHF tests is used to infer both unique flow characteristics within the confinement region and spatial distribution of surface temperature resulting from interactions among the jets.

The new R-134a CHF data is combined with an older FC-72 database obtained at PU-BTPFL by Johns and Mudawar for confined single jet data [22] and multiple jet data (available in [52] but not previously published). The combined database for the two fluids is the basis for a newly recommended CHF correlation.

2. Experimental Methods

2.1. Two-phase Flow Loop

A schematic diagram of the two-phase flow loop used in the present study is shown in Fig. 2(a) and Fig. 2(b) shows a photographic view of the entire experimental facility, with key sub-systems clearly identified. The closed loop conditions the working fluid, R-134a, to the operating conditions required at the inlet of the jet impingement test module and helps maintain flow stability throughout the loop. Liquid refrigerant is pumped through the loop by one of two gear pump (Micropump and Fluid-o-Tech) assemblies, each magnetically coupled to a fan cooled motor. The motors are mounted on vibration dampeners with each powered by a Variable Frequency Drive (VFD) for flow rate control. The two pumps yielded broad but overlapping ranges of flow rate, but both the low and high ranges of flow rate for each pump were avoided to preclude any flow pulsations or instabilities. Two Flow Technology turbine flow meters, FTO and FT series, are used to measure flow rate of subcooled liquid over a range of $1.52 \times 10^{-7} - 6.06 \times 10^{-4} \text{ m}^3/\text{s}$ (0.002 – 8.0 gal/min). Before heading to the jet impingement test module, the flow is routed through a control valve, which is used to regulate the flow resistance, thereby regulating pressure and flow rate as well as helping prevent pressure oscillations in the test module. The liquid acquires heat within the test module, and, depending on the amount of heat supplied, either gains sensible heat or undergoes phase change. The fluid then enters a Trenton fin-and-tube air-cooled condenser, where it rejects heat to the surroundings and returns to single-phase liquid state. A SWEP plate-type heat exchanger is located downstream of the condenser to help achieve subcooled conditions and condense any possible vapor bubbles before the fluid enters the pump. Distilled cooling water is circulated through the other flow side of the heat exchanger with the aid of a Lytron MCS20 modular cooling system.

A set point pressure for the loop is controlled by means of an electrically heated liquid reservoir system at a junction downstream of the condenser. Most of the fluid in the loop is stored in the liquid reservoir, which is fitted with an assembly of heaters and a Lytron MCS20 cooling system. The heaters receive AC power through a solid-state relay controlled by an Omega PID controller based on feedback from a pressure transducer near the junction.

2.2. Test Module

Figs. 3(a) and 3(b) provide, respectively, 3D-CAD exploded and fully assembled views of the jet impingement module. The primary components of the module are a heater block, a jet plate, and housing. Owing to multiple geometries tested in this study,

multiple heater blocks, jet plates and housings were fabricated, but share the same outer dimensions. Machined out of oxygen-free copper (C10100) the heater blocks feature cylindrical bores where high-power-density Watlow cartridge heaters are inserted. The top surface of a particular heater block serves as heating surface in a simulated electronic or power device. Three different heater blocks are used, designated as Small, Medium, and Large, with surface areas of $A_s = 4.23 \times 4.23$, 12.7×12.7 , and $25.4 \times 25.4 \text{ mm}^2$, respectively; Figs. 3(a) and 3(b) show the module containing the Large surface heater. Images of the three heater blocks are shown in Fig. 4(a) both before and after insertion of the cartridge heaters. Fig. 4(b) shows the heater blocks flush mounted into the bottom heater block housings to prevent any flow disturbances to the exit flow. The Small, Medium, and Large heater blocks are fitted with one, four, and nine heaters, respectively, with a layer of boron nitride applied along the outer surfaces of the cartridge heaters to minimize contact resistance. The three heater blocks have holes for one, two, and three thermocouples, respectively, which are drilled 6.35-mm below the top surface. Care was taken to distribute the metal removal evenly around the heater block for a better heat flux distribution.

Twelve different jet plates were machined out of blocks of aluminum alloy 6061, which were then clear anodized to guard against both erosion and corrosion. The plates possess different number of nozzles (1, 3×3 , and 6×6), and jet nozzle diameters of $D_n = 0.40$, 0.79 , and 2.06 mm . The single-jet plate featured one central nozzle and the array-jet plates evenly distributed nozzles located each at the center of each jet cell of the heated surface. The single-jet plates could be used with all heated surfaces, the 3×3 array plates with both the Medium and Large surfaces, and the 6×6 array with only the Large surface. To reduce pressure drop in the jet plate and to ensure flow uniformity, each jet plate has a nozzle made of two parts: an upper enlarged hole (3.175-mm diameter and 12.7-mm deep) and a lower smaller diameter hole with actual jet diameter and depth four times the diameter, Fig. 5(a). A Vee transition between the two holes further helps reduce pressure drop [53], where the Vee-angle equals that of the drill bit used to form the larger hole.

As illustrated in Fig. 3, the housing is made of multiple layers of G-10 and G-7 fiberglass composites assembled together. Both G-10 and G-7 share the same continuous filament glass cloth construction but are impregnated with epoxy and silicone resins, respectively. The inlet plenum housing is shaped to ensure uniform jet velocity through all nozzles. The incoming fluid flow is split into two parts and each enters the module through two ports located on either side of the jet plate, at an angle perpendicular to the impingement direction. A cover plate closes the inlet plenum atop. The jet plate is held between the inlet and outlet plenum housings, with its bottom surface maintaining a fixed confinement height (which is also the jet height) of $H = 4.724 \text{ mm}$. The impingement area is confined between the flat bottom surface of the jet plate and the heater surface. The test module's two outlet plenums provide symmetrical exit of the spent fluid on either side of the impingement area. The heater block is pressed against the heater block housing using a bottom plate, which has small holes to enable electrical connections for the cartridge heaters. The only housing layer that changes between different module configurations is this heater block housing; the three different ones are shown in Fig. 4(b). A glass wool filled gap between the sides of the heater block and its housing helps both minimize heat loss to the ambient and reduce thermal stresses at high temperatures. Calculations prove heat losses are indeed negligible (within 1.49% of electrical power input).

The entire housing is held in place with stainless-steel support braces at the top and bottom, and threaded rods that run the height of the module. To prevent fluid leaks, all solid-solid con-

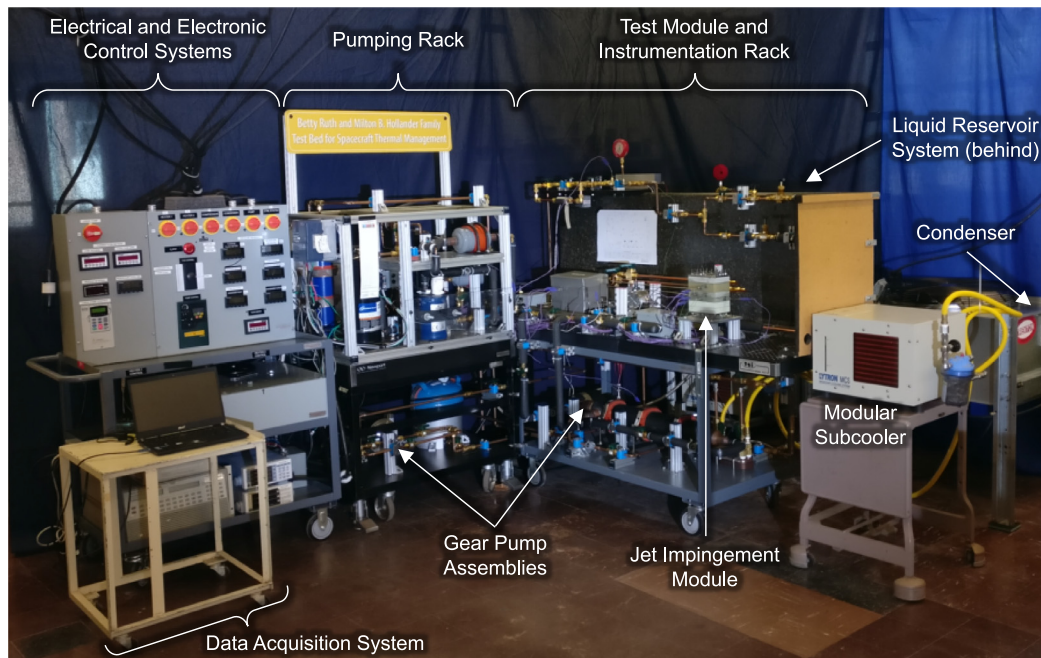
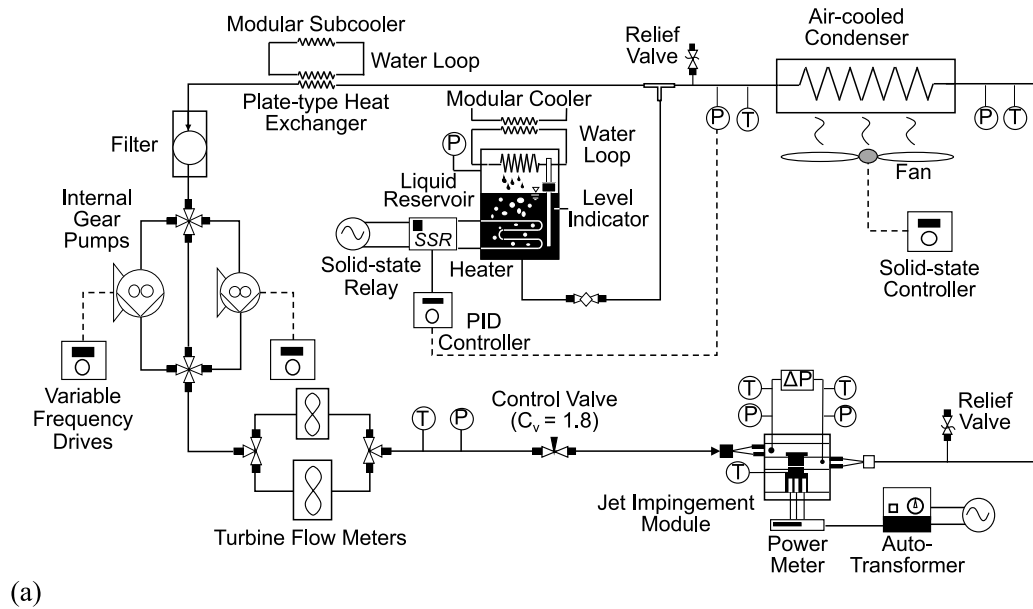


Fig. 2. (a) Schematic diagram of two-phase flow loop. (b) Photographic view of experimental facility indicating key sub-systems.

tacts within the module are provided with Buna-N O-rings coated with silicone grease. Care is taken to apply equal torque to all nuts of the threaded rods so that all the O-rings are uniformly compressed. Electrical power is supplied to the test module's cartridge heaters from a 0–230 VAC autotransformer.

2.3. Instrumentation and Measurement Accuracy

The inlet and outlet plenums of the test module each contains threaded ports for a thermocouple and a pressure transducer junction. Sheathed and grounded type-E Omega thermocouples are used to monitor and measure the fluid temperatures in the inlet and outlet plenums, substrate temperatures in the heater block,

and multiple locations along the flow loop. This thermocouple type is chosen for having the highest Seebeck coefficient and accuracy of all thermocouple types. Pressures in each combination of inlet and outlet plenums are measured with the aid of an Omega MMA absolute pressure transducer and a Honeywell THE differential pressure transducer. Pressures at multiple locations along the loop are monitored using both absolute pressure transducers and analog pressure gauges.

To improve the accuracy of the temperature measurements, all the type-E thermocouples used in the facility are calibrated over a range of -20 to 80°C using a standard platinum Resistance Temperature Detector (Omega Pt 100 1/10 DIN RTD) in a Neslab RTE-220 temperature controlled thermal bath [54]. Deionized water and a

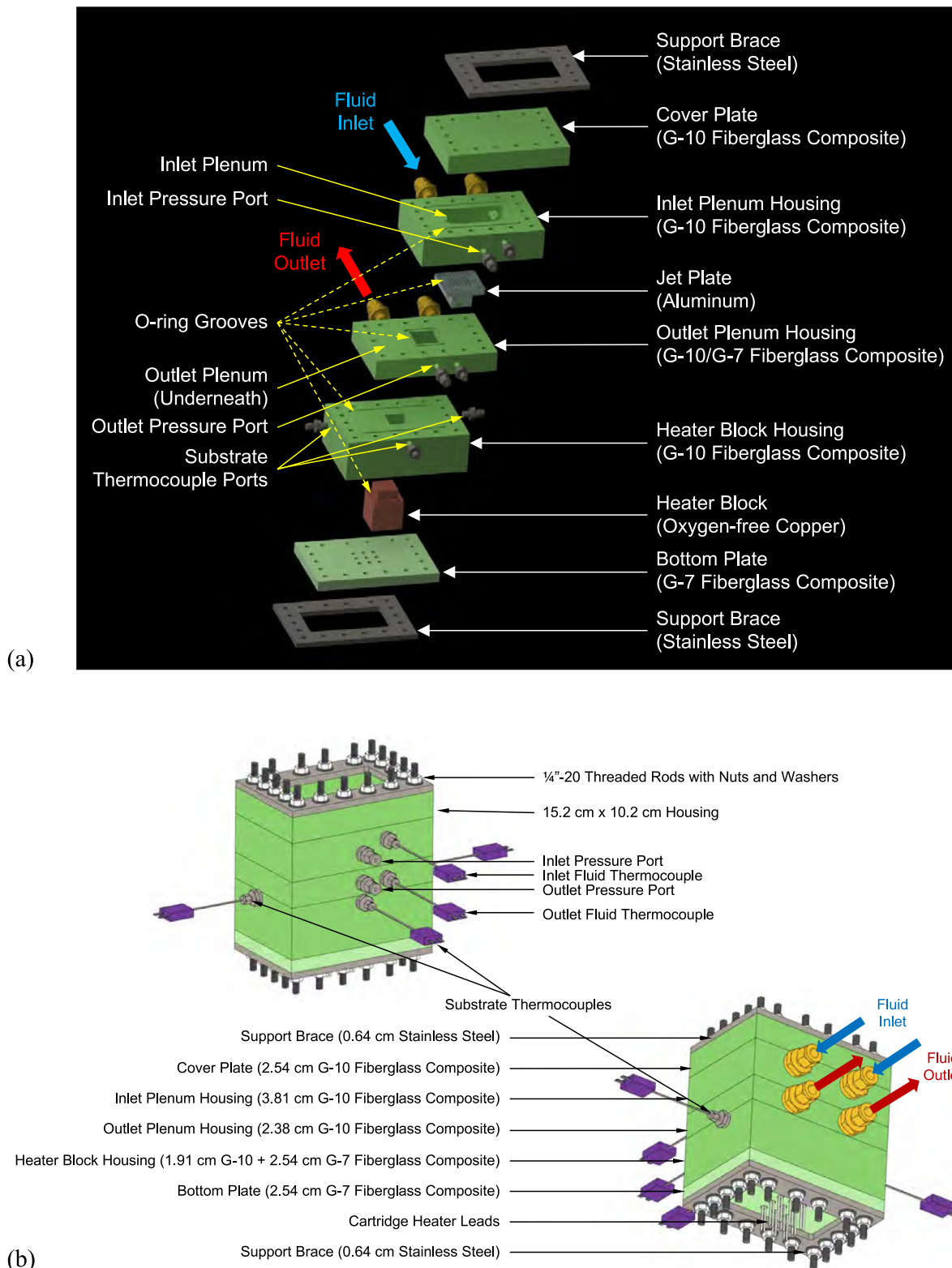


Fig. 3. (a) Exploded 3D CAD view of jet impingement module showing individual components (with Large heating block). (b) 3D CAD view of assembled module.

50-50% vol. ethylene glycol-water mixture are used as bath fluids above and below 7.5°C, respectively. During the calibration, the thermocouples and RTD are immersed with their tips close to each other near the middle of the bath and readings taken in 2.5°C intervals after steady state conditions were reached. Temperature readings of the RTD are obtained from their resistance outputs us-

ing the European curve (ITS-90, $\alpha = 0.00385 \Omega/\Omega/^\circ\text{C}$). Thermocouple and RTD temperatures are finally correlated against each other using 4th-order polynomials. This procedure resulted in all the thermocouples calibrated to within $\pm 0.1^\circ\text{C}$.

Volumetric flow rate is measured by one of the two turbine flow meters. The voltage, current, and power input to the cartridge

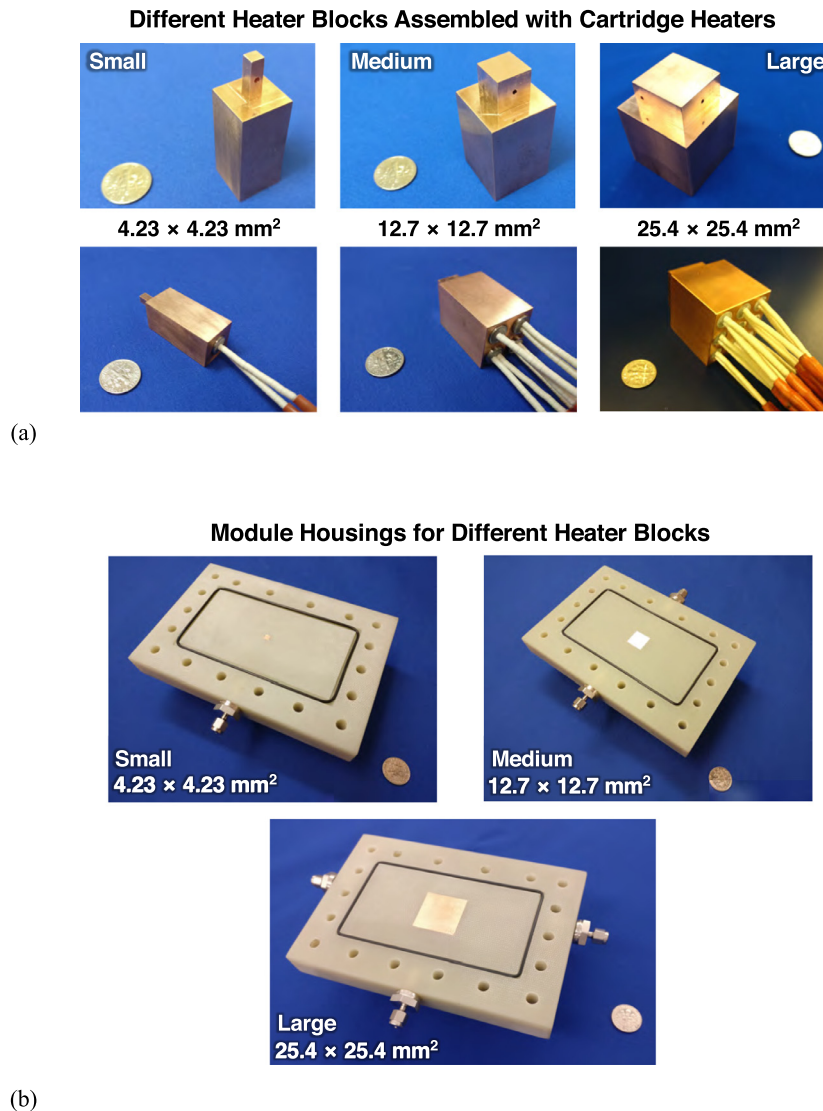


Fig. 4. (a) Photographs of different heater blocks assembled with cartridge heaters, and (b) corresponding module housings indicating thermocouple ports. A United States dime is included as a size reference.

heaters are measured using a Yokogawa WT310 power meter. Liquid level in the reservoir is monitored using a Gems XT-800 float-type sensor. Electronic signals from all the sensors are collected with the aid of an FET multiplexer and measured by an integrating voltmeter of an HP data acquisition system. The measured readings are monitored and recorded on a computer using LabVIEW software. Efforts are taken to suppress electrical noise in the analog electronic signals using a combination of line reactors, toroidal inductors, and specialized VFD cables.

Maximum uncertainties in the measurements of temperature, absolute pressure, differential pressure, volume flow rate, and heat input are $\pm 0.1^\circ\text{C}$, $\pm 0.1\%$, $\pm 0.1\%$, $\pm 0.15\%$, and $\pm 1.49\%$, respectively. By considering a conservative $\pm 1\%$ uncertainty in length measurements, the maximum uncertainty in heat flux is determined to be $\pm 2.05\%$. The maximum uncertainty in q''_{CHF} is determined to be $\pm 4.35\%$, which is comprised of both heat flux measurement uncertainty and CHF isolation error (see [section 2.4](#)).

2.4. Operating Procedure

A summary of the geometrical parameters and operating conditions parameters of the study is provided in [Table 1](#). Prior to a

day's testing, the electrical and electronic control systems as well as the data acquisition system are turned on. All valves in the flow loop are then opened, and both the modular coolers and the condenser are turned on. The PID controller is set to a particular saturation pressure and the system allowed to reach a steady state. This brings the module's inlet subcooling to the desired value for a constant inlet temperature. Based on the flow rate for a given test, one combination of gear pump and turbine flow meter are selected and valves leading to the other combination are closed. The pump is started and set to a particular flow rate. Power is supplied to the module's cartridge heaters by adjusting the autotransformer in a stepwise fashion. Heat flux increments are coarse at the beginning, around 4 – 8 and 8 – 16 W/cm^2 for the single-jet and jet array configurations, respectively. The increments are reduced to a maximum of $\sim 5 \text{ W}/\text{cm}^2$ close to CHF for the higher CHF cases, and even smaller increments for the lower CHF cases. Steady state conditions are achieved for each heat flux increment and all relevant data recorded. The module is rigidly mounted away from potential sources of vibration to preclude influencing the fluid flow inside the module or inducing CHF prematurely. CHF occurrence is verified by an unsteady rise in the heater block's temperature following a heat flux increment. This rise takes place in one of two

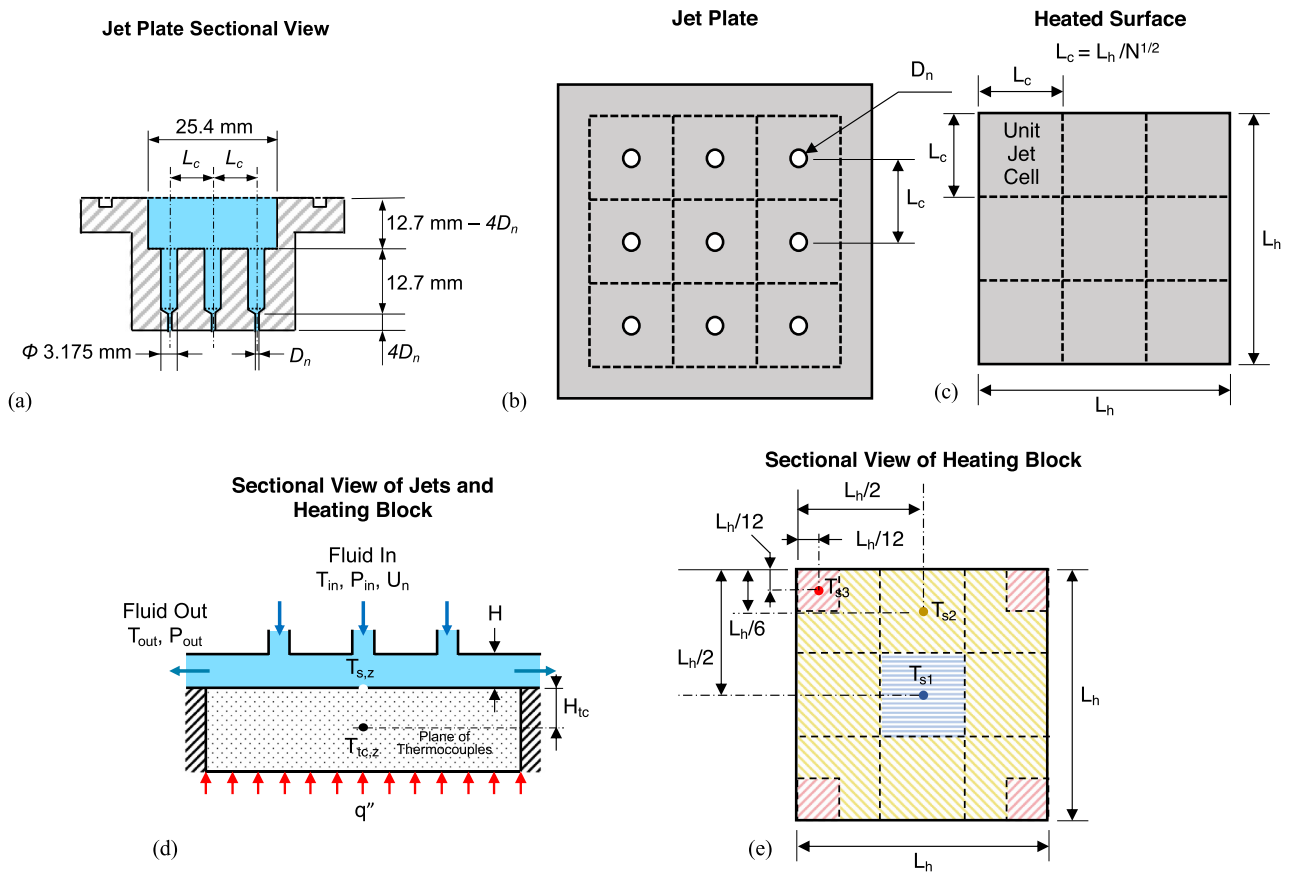


Fig. 5. Sectional views of nozzles and heated surface illustrating procedure for determining average surface temperature for a 3×3 jet array impinging on the Large surface: (a) sectional view of jet plate, (b) top view of the jet plate, (c) top view of heated surface, (d) sectional view of jets and heating block, and (e) thermocouple measurements used to determine average surface temperature.

Table 1
Summary of experimental parameters.

Varied parameters	
Number of jets, N	1, 3×3 , 6×6
Diameter of nozzle, D_n	0.40, 0.79, 2.06 mm
Heated surface area, A_s	$25.4 \times 25.4 \text{ mm}^2$ (Large), $12.7 \times 12.7 \text{ mm}^2$ (Medium), $4.23 \times 4.23 \text{ mm}^2$ (Small)
Jet nozzle velocity, U_n	0.5, 1 – 10 m/s (in increments of 1 m/s)
PID set pressure	88.2, 99.4, 111.7 psia (608,118, 685,339, and 770,144 Pa with T_{sat} of 22.0, 26.0, and 30.0°C, respectively)
Heat flux, q''	0 – 100% q''_{CHF}
Fixed parameters	
Jet Height, H	4.724 mm

forms: (i) a sudden sharp increase or (ii) a mild never-ceasing temperature increase; details of both are discussed later in section 3.6. CHF is calculated as the average of heat flux causing CHF initiation and the preceding heat flux, which brings maximum error in CHF detection to $\sim 2.5 \text{ W/cm}^2$, with error for majority of the cases $\sim 1\%$. All other measured parameters correspond to the steady state heat flux setting preceding CHF. To prevent permanent damage to the module, power input to the cartridge heaters is disconnected shortly after CHF is detected or once the heater block exceeds 150°C ; the latter was mainly observed in the 6×6 jet array tests involving higher saturation pressures and jet velocities. Eventually, the heater block is allowed to cool down and the process repeated for another set of operating conditions.

After all desired operating conditions for a given module configuration are completed, the module is reassembled with different components and a clean heat transfer surface, and the operating procedure repeated. It should be noted that certain combinations of parameters in Table 1 could not be tested because of limitations of the test facility.

2.5. Data Processing

After reaching steady state for each test case, at least 150 s of recorded data is averaged to obtain a steady state datapoint. Fig. 5 includes schematic diagrams illustrating the data reduction procedure for a 3×3 jet array impinging on the Large surface for example; other configurations are tackled in a similar manner. As illustrated in Figs. 5(b) and 5(c), the entire heated surface can be divided into equal square jet cells of side length L_c . The jet plate contains nozzles of orifice diameter D_n separated from one another by the same length. As shown in Fig. 5(d), all heater block thermocouples are mounted in the same plane at a distance of $H_{tc} = 6.35 \text{ mm}$ below the impingement surface. These local temperature measurements, $T_{tc,z}$, are first translated into temperatures on the impingement surface, $T_{s,z}$. A study by Wadsworth and Mudawar [53] analyzed this problem for a jet impingement heater block and determined a basic one-dimensional heat conduction model was adequate. With a constant heat flux from the bottom and perfect insulation on the sides, this is achieved according to

Table 2
Summary of key parameters of CHF datapoints.

Critical heat flux, q''_{CHF}	16.88 – 222.84 W/cm ²
Inlet plenum pressure, P_{in}	612,731 – 870,152 Pa(88.87 – 126.20 psia)
Saturation (outlet) pressure, P_{sat}	612,202 – 837,410 Pa(88.79 – 121.46 psia)
Saturation temperature, T_{sat}	22.23 – 32.94°C
Inlet temperature, T_{in}	17.20 – 25.03°C
Inlet subcooling, $\Delta T_{sub,in}$	1.50 – 13.03°C
Average surface temperature, T_s	36.45 – 128.20°C
Outlet temperature, T_{out}	21.86 – 30.76°C
Mass flow rate, \dot{m}	7.057×10^{-4} – 0.179 kg/s
Volumetric flow rate, Q_v	5.75×10^{-7} – 1.46×10^{-4} m ³ /s(0.009 – 2.314 gal/min)
Jet nozzle velocity, U_n	0.498 – 10.076 m/s
Inlet quality, $x_{e,in}$	-0.112 – -0.012
Outlet quality, $x_{e,out}$	-0.077 – 0.846

the relation

$$T_{s,z} = T_{t,c,z} - \frac{q'' H_{tc}}{k_s}, \quad (2)$$

where k_s is the thermal conductivity of the heater block. The average surface temperature, T_s , is then determined by an area weighted averaging the local surface values,

$$T_s = \frac{\sum A_z T_{s,z}}{A_s}, \quad (3)$$

where A_z is as the area of an evenly-divided square unit cell centered where $T_{s,z}$ is determined. For the Large surface, with three local temperature measurements, an illustration of the area-weights for each local temperature is shown in Fig. 5(e). For example, the central region (shaded in blue) is dominated by T_{s1} (shown in blue). The average surface temperature for this surface reduces down to $T_s = (T_{s1} + 7T_{s2} + T_{s3})/9$.

All thermophysical properties of R-134a are obtained from NIST-REFPROP [55]. The saturation pressure used to calculate all saturation properties is the measured outlet plenum pressure, i.e., $P_{sat} = P_{out}$ [22,39]. This is justified by the much smaller pressure drop between the impingement area to outlet compared to that between the inlet and outlet plenums [39]. The outlet fluid enthalpy is determined by an energy balance for the impingement area,

$$h_{out} = h_{in} + \frac{q'' A_s}{\dot{m}}, \quad (4)$$

where \dot{m} is the total mass flow rate of R-134a. Thermodynamic equilibrium qualities at the inlet and outlet are calculated as

$$x_e = \frac{h - h_f}{h_{fg}}, \quad (5)$$

where $h = h_{in}$ or h_{out} , and both h_f and h_{fg} are based on P_{sat} . Inlet subcooling is determined as $\Delta T_{sub,in} = T_{sat} - T_{in}$. Key parameter ranges corresponding to CHF datapoints for all tested configurations of the study are provided in Table 2. It is to be noted that these values represent all tested module configurations.

3. Experimental Results and Discussion

3.1. Jet Impingement Boiling Curve

Fig. 6 shows a representative boiling curve for the 3×3 jet array impinging on the Large surface and indicated set of operating conditions. The fluid is injected from the nozzles in subcooled state and only gains sensible heat for heat fluxes corresponding to the single-phase liquid cooling regime, characterized by a constant heat transfer coefficient and therefore constant slope. This regime is terminated at the Onset of Nucleate Boiling (ONB), once liquid in the wall layers emanating from the impingement zones acquire sufficient superheat to allow bubbles to begin nucleating

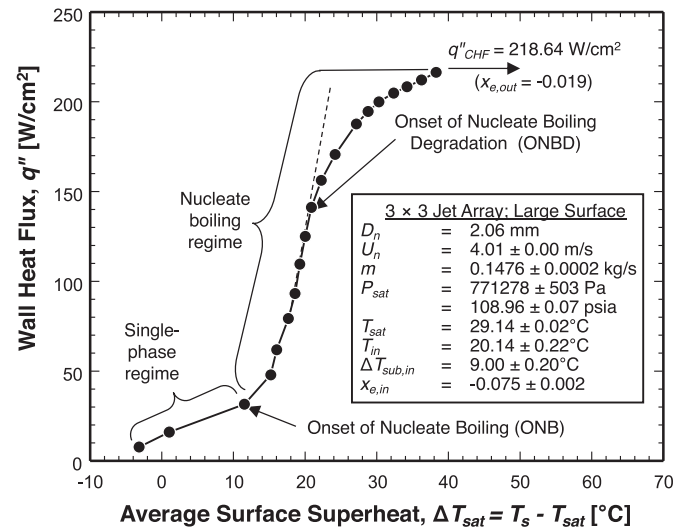


Fig. 6. Representative confined jet impingement boiling curve indicating different heat transfer regimes and transition points.

on the heated surface; this is also where the boiling curve incurs an appreciable increase in slope. The temperature corresponding to ONB, $T_{s,ONB}$, is about 10.5°C higher than T_{sat} . In the nucleate boiling regime, increases in heat flux produce much smaller increases in surface temperature compared to the single-phase regime as the heated wall energy is increasing being dissipated by the coolant's latent than sensible heat [56]. Overall shape of the boiling curve at the lower region of nucleate boiling is similar to that seen in literature for other fluids [39,57]. However, there is pronounced decline in slope in the upper region at the point of Onset of Nucleate Boiling Degradation (ONBD) occurring over a sizeable fraction of the nucleate boiling heat flux range starting at 141.22 W/cm²; this degradation is attributed to coalescence of bubbles into larger vapor masses. In pool boiling and many flow boiling situations, this point is much closer to the CHF point. But in jet impingement, with the liquid jet introduced directly onto the heated surface, liquid is better able to continue breaking through the vapor masses and contact the surface, thereby delaying CHF occurrence, albeit at the cost of increasing surface temperature. The effectiveness of this contact varies with operating conditions, and CHF has been observed in prior studies to occur at portions of the surface not directly impacted by the jets [39]. Overall, the broad extent of the upper region of nucleate boiling is attributed to the ability of the fast moving wall layers emanating from the impingement zones to provide continued liquid access to the surface, yielding much higher CHF values than with pool boiling [58,59]. As indicated in Fig. 6, CHF is detected as an uncontrollable increase in surface temperature, occurring at 218.64 W/cm².

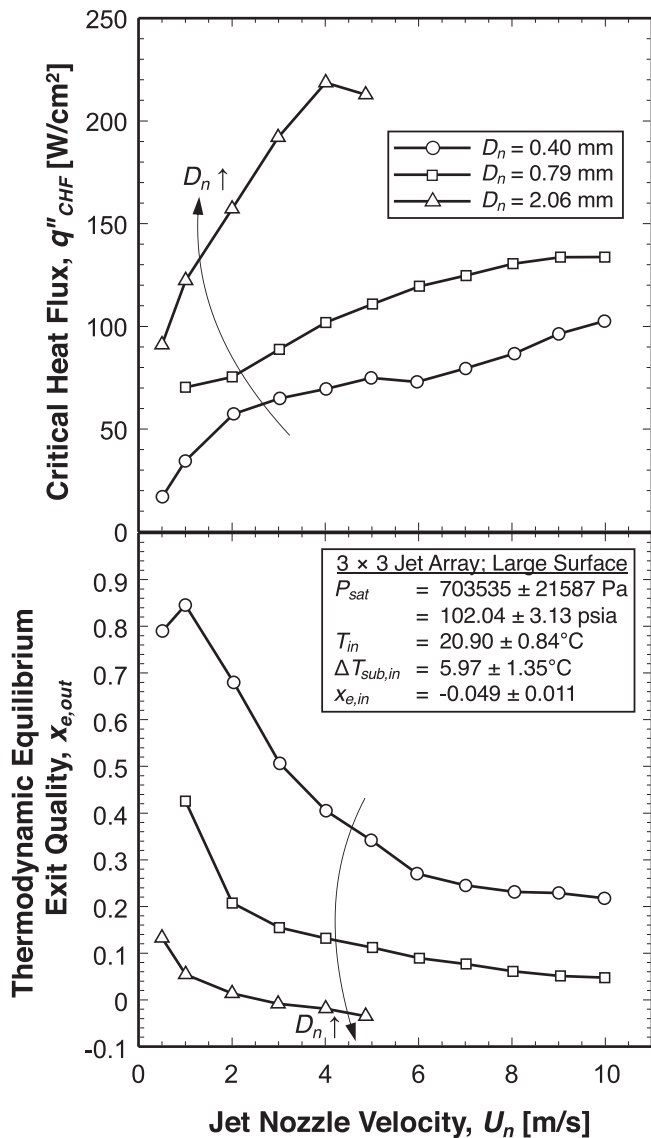


Fig. 7. Variations of CHF and corresponding thermodynamic equilibrium exit quality with jet nozzle velocity for nozzle diameters of $D_n = 0.40, 0.79,$ and 2.06 mm.

It should be noted that the extended degradation region preceding CHF has also been observed in prior PU-BTPFL jet impingement studies [21,22,27,39,60]. The present boiling curves are also similar in shape to those measured by Copeland [61]. Some other works of jet impingement [62] have provided similar interpretations of ONBD and CHF.

However, different interpretations have been used in regards to which point of the boiling curve represents true CHF. For instance, while not always explicitly in publications, Katto's team identified the heat flux corresponding to ONBD as CHF (this is based on private communication between one of the present authors and Prof. Y. Katto around 1995). Browne *et al.* [63] and Shin *et al.* [64] also appear to terminate their boiling curves at ONBD, which they defined as point of temperature excursion, perhaps to protect their heaters against physical burnout should the actual CHF point be reached. Similarly, Nakayama *et al.* [65] defined CHF as the condition in which a rapid local temperature rise was observed, but their boiling curves depict a coincidence of ONBD and CHF.

Overall, it must be pointed out that distinguishing ONBD from CHF in the manner depicted in Fig. 6 is of paramount importance to jet impingement given the large heat flux extent between the two points.

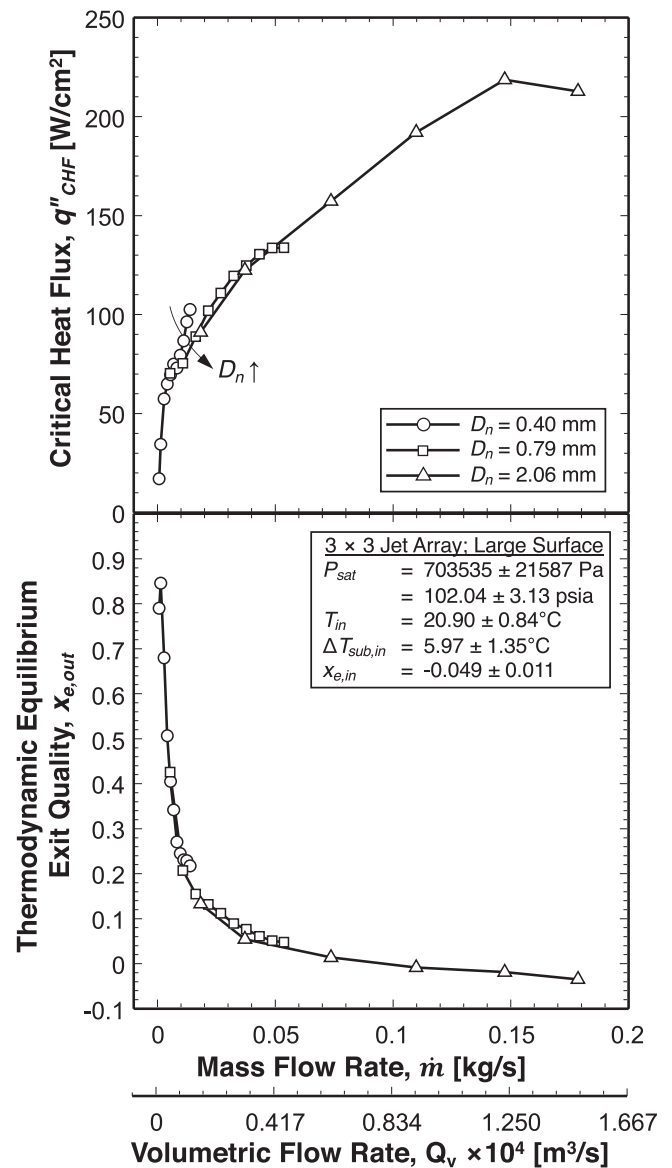


Fig. 8. Variations of CHF and corresponding thermodynamic equilibrium exit quality with total mass flow rate for nozzle diameters of $D_n = 0.40, 0.79,$ and 2.06 mm.

3.2. Effects of Jet Velocity

Fig. 7 shows variations of CHF and the corresponding thermodynamic equilibrium exit quality, $x_{e,out}$, with jet velocity, U_n , for nozzle diameters of $D_n = 0.40, 0.79,$ and 2.06 mm. CHF is shown increasing monotonically with increasing U_n (excepting in a non-linear fashion). The velocity effect on CHF appears stronger in the lower velocity range. Although prior studies (e.g., [39]) have reported a decrease in CHF with increasing velocity above a certain velocity value, this was only observed in the present study at $U_n = 4.87$ m/s and $D_n = 2.06$ mm, Fig. 7, which should not be interpreted as a generalized trend. Overall, the increase in CHF with increasing D_n for a fixed U_n is easily attributed to the increase in coolant flow rate, while the increase with increasing U_n for a fixed D_n is closely associated with better ability of a faster moving wall layer fluid to break through coalescent vapor masses and maintain liquid access to the surface.

Knowledge of the thermodynamic equilibrium exit quality is important to understanding the fluid state along the heated surface, which can have appreciable impact on CHF mechanism. A

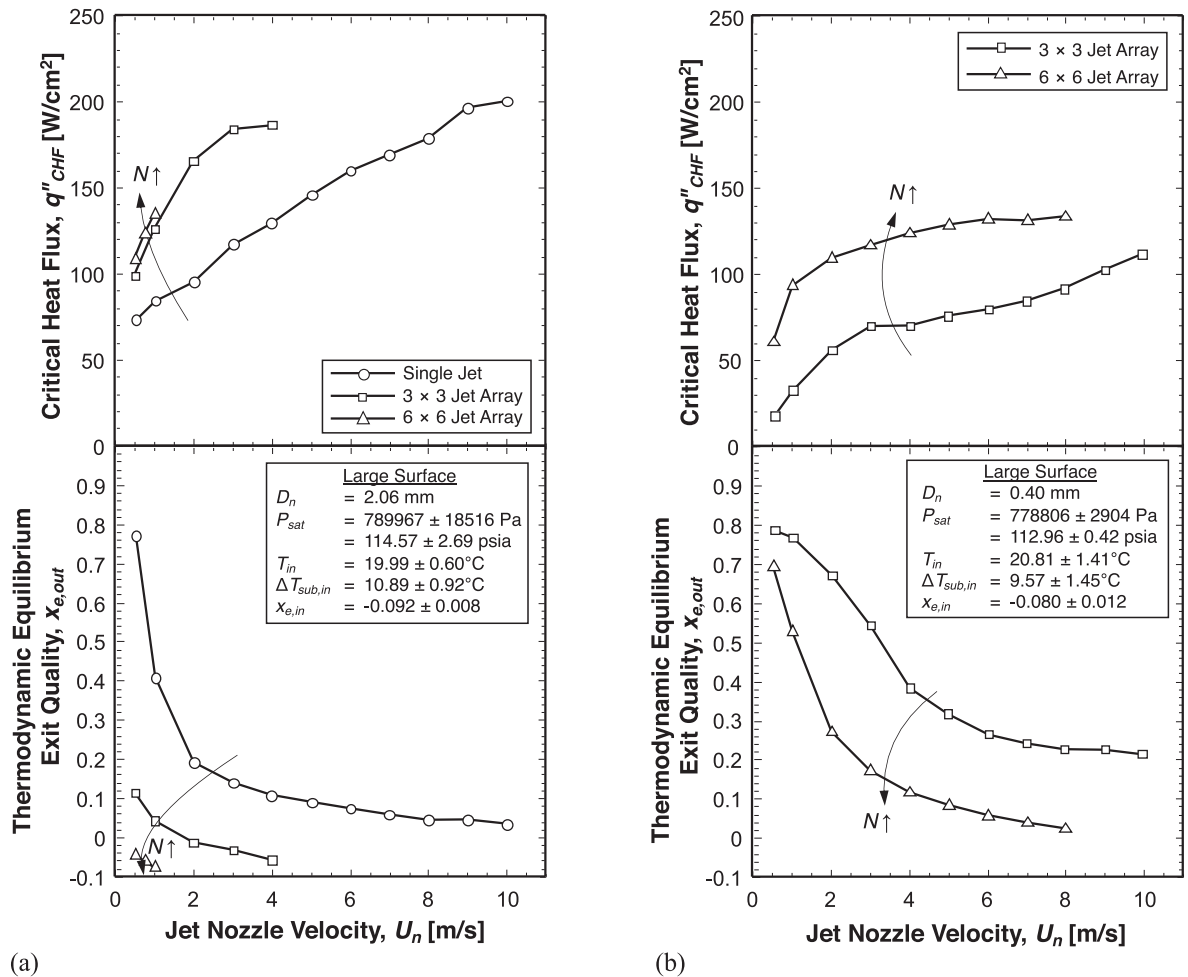


Fig. 9. Variations of CHF and corresponding thermodynamic equilibrium exit quality with nozzle velocity for a single jet, 3×3 array and 6×6 array, with nozzle diameters of (a) $D_n = 2.06$ mm, and (b) $D_n = 0.40$ mm.

negative value of $x_{e,out}$ indicates a 'subcooled CHF' mechanism and a value between 0 and 1 'saturated CHF'. With the inlet quality maintained fairly constant for all cases, higher values of $x_{e,out}$ amount to a large void fraction and vice versa. Figure 7 indicates $x_{e,out}$ is very high at the lower jet velocities, reaching a value of 0.846 at 1 m/s for $D_n = 0.40$ mm. This means a large amount of vapor is present over the surface at lower velocities, and a larger fraction of the coolant's latent heat is utilized. The decrease in $x_{e,out}$ with increasing D_n for a fixed U_n evident in Fig. 7 is directly related to the increasing mass flow rate. Like the CHF trends, those for $x_{e,out}$ are also not linear, with a sharper decrease in $x_{e,out}$ observed in the lower velocity range, and becoming fairly constant at higher velocities. Notice that CHF is encountered in some operating conditions while the fluid is still in subcooled state, which is indicated by negative $x_{e,out}$ values. For instance, the case of $U_n = 5$ m/s and $D_n = 2.06$ mm is shown yielding a subcooled CHF with $x_{e,out} = -0.035$. Such conditions point to the important role of condensation in the subcooled bulk fluid in helping collapse vapor bubbles, allowing the fluid to exit in liquid state. Notice also that these conditions yield the highest CHF values in Fig. 7. Overall, the combination of high CHF and pure liquid at the module outlet is very desirable for thermal management system operation not only in terms of superior cooling performance but also ability to utilize a simple single-phase liquid cooling loop rather than a two-phase loop [22].

3.3. Effects of Jet Diameter

In addition to addressing the effects of jet velocity, Fig. 7 provided useful information concerning effects of nozzle diameter as well. Increasing D_n for a fixed jet velocity has implications of (i) increasing the flow rate, (ii) producing a larger stagnation region, and (iii) increasing the jet's ability to spread more uniformly within its cell. By increasing D_n from 0.40 to 2.06 mm, the same figure shows CHF is increased by factors of 5.32 and 3.14 for jet velocities of 0.5 and 4 m/s, respectively. This shows D_n has a stronger effect on CHF for slower jets. The same figure shows $x_{e,out}$ decreases with increasing D_n over the entire velocity range, with the strongest influence seen at lower velocities. For smaller diameters, $x_{e,out}$ decreases by a large amount with increasing U_n when compared to larger diameters. For diameters of 0.40 and 2.06 mm, $x_{e,out}$ decreases by 0.385 and 0.151 for an increase in U_n from 0.5 to 4 m/s, respectively.

A more insightful way of presenting the same data is show variations of CHF and $x_{e,out}$ against mass flow rate and also volumetric flow rate. As shown in Fig. 8, CHF generally increases with increasing flow rate. For a particular jet array and moderate flow rate, CHF is slightly higher for smaller D_n because of higher U_n . This highlights a stronger dependence of CHF on U_n than on flow rate. But it should also be mentioned that pressure drop increased almost proportionally to the square of the velocity. This means that, for a particular flow rate, pumping power is much higher for smaller D_n

even though they yield slightly higher CHF. Figure 8 also shows, as expected, $x_{e,out}$ decreases monotonically with increasing flow rate and this decrease is more pronounced for smaller flow rates.

3.4. Single Jet versus Jet Arrays

Figure 9 shows variations of CHF and $x_{e,out}$ with U_n for a single jet and 3×3 and 6×6 jet arrays. The results are shown for two different jet diameters, $D_n = 2.06$ and 0.40 mm, in Figs. 9(a) and 9(b), respectively. For $D_n = 2.06$ mm, Fig. 9(a) shows both arrays yield better CHF values than those for the single jet. This advantage of the arrays is attributed to both abundant liquid supply for a fixed U_n as well as more uniform introduction of liquid onto the heated surface. For instance, at $U_n = 3$ m/s, CHF increases by 57.39% with the 3×3 array compared to that for the single jet. However, this advantage comes at the price of an eight-fold increase in flow rate, which has serious implications as far as size of the external fluid handling loop is concerned. Because of the increase in flow rate, Fig. 9(a) also shows $x_{e,out}$ decreasing with increasing U_n , and more so with increasing jet number.

For the smaller diameter, $D_n = 0.40$ mm, Fig. 9(b) shows separation between CHF curves for 3×3 and 6×6 arrays remains fairly constant for all jet velocities, meaning the percentage augmentation in CHF is higher at lower velocities. For example, compared to the 3×3 array, the 6×6 array provides 185.20% and 45.88% CHF improvements for jet velocities of 1 and 8 m/s, respectively. But, here too, this improvement comes at the cost of a three-fold increase in flow rate.

Overall, Figs. 9(a) and 9(b) prove the CHF improvement with increasing jet number is more pronounced for the smaller jet diameter and lower velocities. This might be attributed to the fact that, because of a smaller spread of the wall jets for smaller diameters and lower velocities, more jets are needed to cover and effectively cool the entire surface.

Plotting the cases from Fig. 9(a) against total mass flow rate and volumetric flow rate provided added insight into overall cooling system implications, especially pumping requirements. Shown in Fig. 10, a decrease in jet number for a given flow rate enhances CHF. This implies that for situations involving stringent flow rate limits, a single jet provides better CHF performance than jet arrays having the same D_n . This advantage can be explained by the single jet acquiring much higher U_n for the same flow rate, thereby helping the wall jet to maintain better contact with the surface and for a longer distance from the impingement zone. For example, for the same mass flow rate of 0.073 kg/s, the 3×3 array yields 52.38% higher CHF value than the 6×6 array. This does prove that jet velocity has a stronger influence on CHF than total flow rate. But, as indicated earlier, the increase in U_n also leads to appreciable increases in pressure drop and pumping power.

3.5. Effects of System Saturation Pressure

Most prior jet impingement works [21,22,39] investigated the effects of inlet subcooling on CHF for different fluids (e.g., water and FC-72) at a constant saturation pressure. Systems utilizing these fluids are often operated at fixed pressures slightly higher than atmospheric. This means inlet subcooling can be easily adjusted by controlling fluid inlet temperature alone. For reference, T_{sat} values for water and FC-72 at atmospheric pressure are 99.98 and 56.56°C , respectively, and CHF for these fluids has been shown to improve appreciably by increasing inlet subcooling [22,24,39]. However, low-boiling-point fluids like R-134a pose a crucial challenge when used in pumped loops (as opposed to vapor compression systems). For R-134a, saturation temperatures corresponding to $100,000$ Pa (14.50 psia) and $600,000$ Pa (87.02 psia) are -26.36 and 21.57°C , respectively. Therefore, at room temperature, fluid in

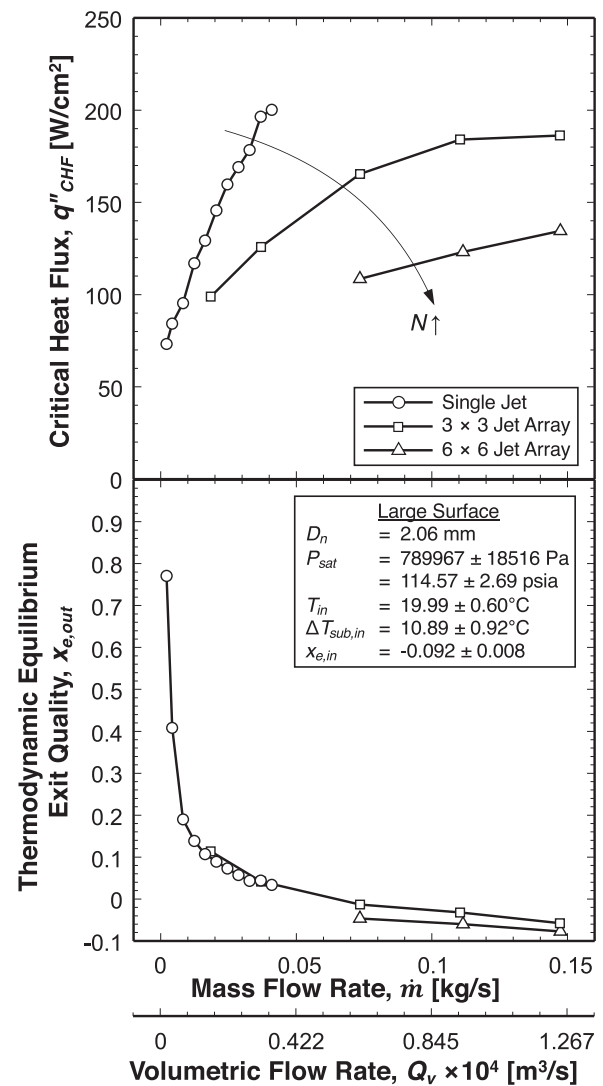


Fig. 10. Variations of CHF and corresponding thermodynamic equilibrium exit quality with total mass flow rate for a single jet, 3×3 array and 6×6 array with $D_n = 2.06$ mm.

the system is already at saturated state with a high system pressure. In this situation, subcooled conditions at the inlet to the test module can be achieved by either decreasing the inlet pressure or increasing the system pressure. As discussed in Section 2.1, a liquid reservoir system is required to adjust the system's 'stiffness' in order to avoid flow loop instabilities [66]. This component system is also used to set the system saturation pressure while inlet pressure is regulated by the pump and main control valve in order to vary the inlet subcooling. A somewhat similar technique was employed by Vader *et al.* [58] for liquid nitrogen jets, where a non-condensable gas – helium – was mixed in the fluid to increase saturation pressure. It should be noted that controlling the subcooling by adjusting the saturation and inlet pressures using the present pumped loop system eliminates the need for a separate refrigeration system to chill the fluid below room temperature before entering the module. Incorporating a refrigerated chiller would greatly increase size, weight and cost of the thermal management system [58].

Variations of CHF and $x_{e,out}$ with U_n for different saturation pressures, and therefore different subcoolings, are shown for a single jet with $D_n = 2.06$ mm and 3×3 jet array with $D_n = 0.40$ mm in Figs. 11(a) and 11(b), respectively. Both configurations show

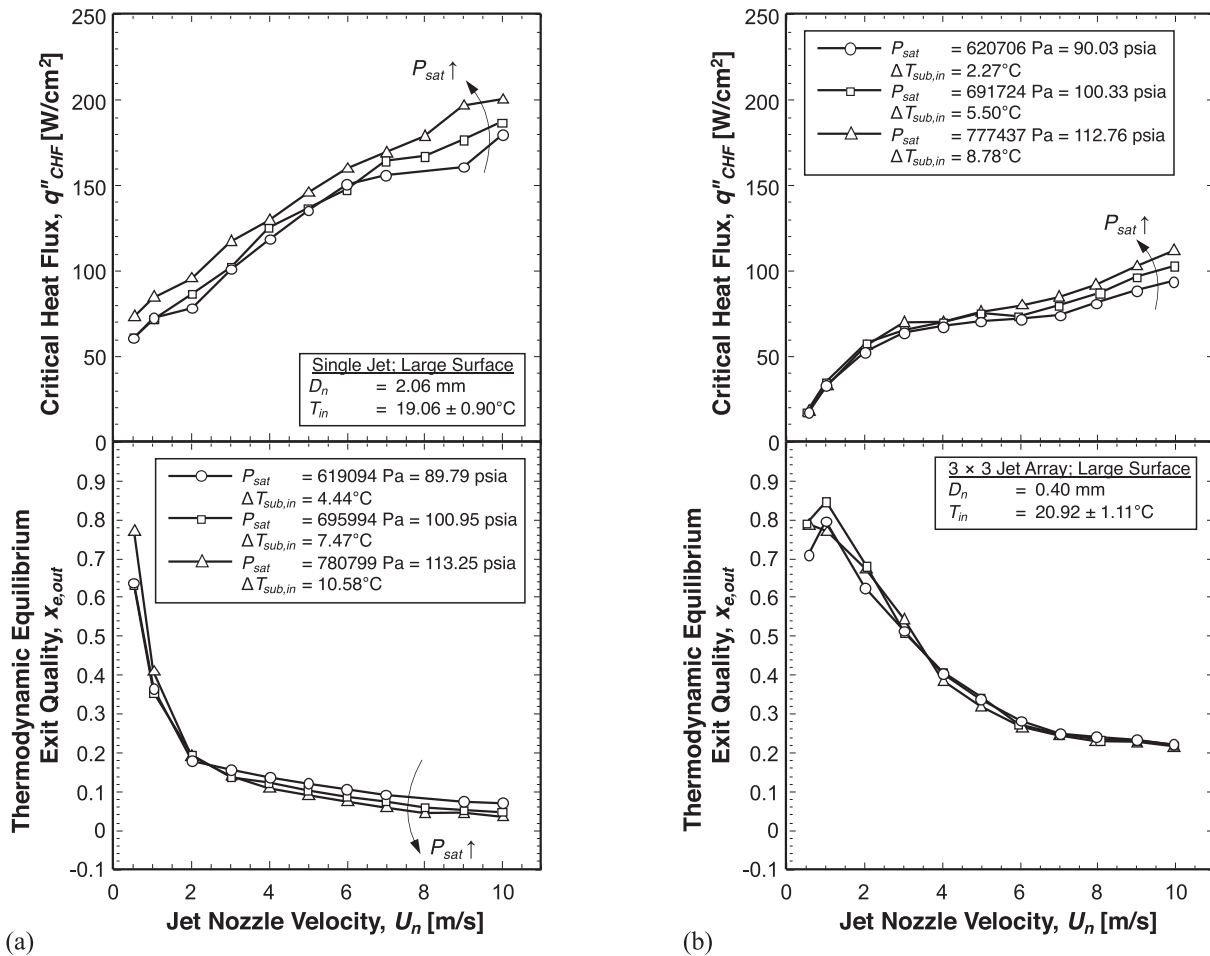


Fig. 11. Variations of CHF and corresponding thermodynamic equilibrium exit quality with nozzle velocity for different saturation pressures for (a) a single jet with $D_n = 2.06$ mm, and (b) 3×3 array with $D_n = 0.40$ mm.

minimal effects of P_{sat} on CHF when compared to the other parameters tested. For the single jet, CHF increased fairly linearly with increasing U_n , with higher saturation pressures providing some improvement by virtue of the higher inlet subcooling. For the 3×3 jet array, on the other hand, better CHF improvement is realized at higher jet velocities; but here too increasing saturation pressure (also inlet subcooling) provides some improvement. Overall, the CHF improvements resulting from the increased saturation pressure is limited by the relatively limited increase in inlet subcooling. For example, for the 3×3 array with $D_n = 0.40$ mm and $U_n = 10$ m/s, increasing the saturation pressure from 620.7 to 777.4 kPa increases the inlet subcooling by only 7.60°C , which explains the rather modest increase in CHF of 19.26%.

Figures 11(a) and 11(b) show no appreciable differences in $x_{e,out}$ among the different saturation pressures. As P_{sat} is increased with a fixed inlet temperature, the corresponding saturation temperature increases, meaning that the fluid needs to gain more sensible heat to reach saturation conditions. This is manifest in experiments as a higher steady state surface temperature for a particular heat flux, leading to obvious differences in the nucleate boiling region of the boiling curve [58].

3.6. Temporal CHF Trends

All studies in jet impingement literature define CHF as the point where a surface temperature excursion is observed, albeit the details vary as discussed in Section 3.1. This section further clarifies

this issue using temporal records of select CHF cases. Over the course of many test cases, two significantly different types of CHF were encountered: a sudden sharp CHF excursion and a mild prolonged CHF excursion. The former was generally noticed at lower flow rates and the latter at higher flow rates, with other jet parameters such as jet diameter, number, and velocity not seeming to influence the excursion type.

Both types fall under the fundamental depiction of CHF as an uncontrollable (unsteady) increase in surface temperature following a small increase in heat flux. One example of each type is shown in Fig. 12 in the form of temporal records of the thermocouples embedded in the heating block. The case to the left corresponds to a relatively low mass flow rate of 0.0028 kg/s and the one on the right to a 15.5-fold higher mass flow rate of 0.0434 kg/s. For both cases, $t = 0$ s corresponds to the last steady state boiling condition preceding CHF. At this instant, heat flux for both cases is increased by around 4.5 W/cm^2 . The system responds to this increase with a corresponding increase in the heater block temperature. For both cases, the temperature increase appears to subside around 300 s but continue to rise thereafter.

Temperatures in the case to the left increased gradually until around 1000 s before rising very sharply, prompting the operator to quickly turn off electrical power input to the cartridge heaters to safeguard the module. This kind of sharp excursion is exceptionally dangerous as the heater block temperature can reach dangerous highs of a few hundred $^\circ\text{C}$ in a few seconds if unchecked. The time at which the excursion began to escalate varied from case to

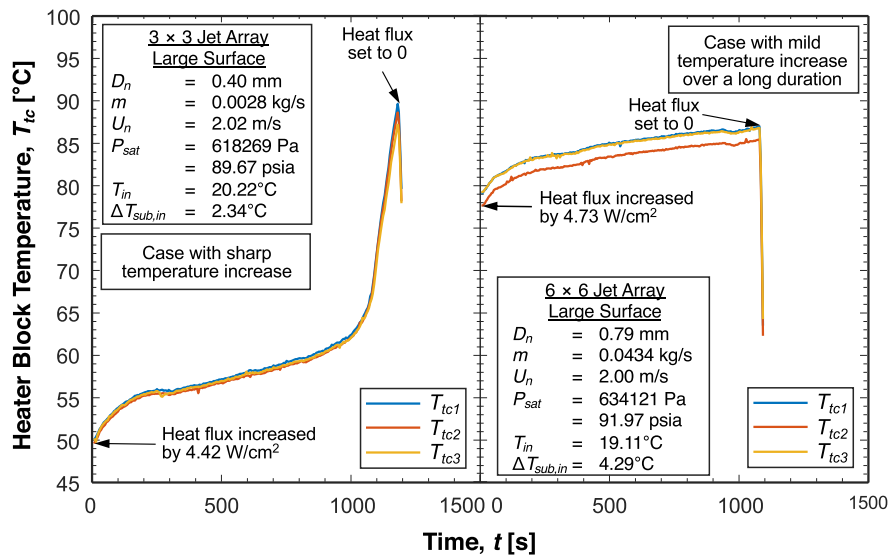


Fig. 12. Temporal thermocouple records indicating two types of CHF: a sudden sharp CHF at lower flow rates (left), and a mild prolonged CHF at higher flow rates (right).

case and, in a few cases, occurred immediately after incrementing the heat flux. Overall, this type of excursion provides an unquestionable measurement of true value of q''_{CHF} .

On the other hand, temperatures in the case to the right of Fig. 12, which correspond to the higher flow rate, do not exhibit a sharp excursion but rather a mild never-ceasing temperature increase. With no tendency to attain steady state, the heat flux is eventually set to zero. Validity of CHF detection for the slow excursion was validated in initial tests where temperatures were allowed to continue the gradual increase for a couple of hours.

The differences in CHF type can be directly attributed to two-phase flow structure within the confinement space above the heating surface. Although the different geometrical configurations considered in this study are shown to influence CHF to various degrees, the confinement height, H , is kept the same. This is a design decision based on findings from previous studies which showed H has virtually no effect except for very small heights [22,38,39,67]. In the present tests, all the fluid impinging on the surface is diverted in two opposite directions to the outlet plenums. With the plenum width being constant, the total rectangular flow area ($H \times$ plenum width) on either side remains the same for all the tests. This means the average velocity of fluid exiting the two opposite outer edges of the heated surface would increase with increasing mass flow rate. At lower mass flow rates, the exit velocity is small and both exit quality and exit void fraction are large. Therefore, at CHF, vapor is able to coalesce into relatively large masses that effectively insulate the heating surface, causing most of the heat from the cartridge heaters to be dissipated within the copper heating block, and resulting in sharp temperature escalation.

On the other hand, at high mass flow rates, the exit velocity is high and both the exit quality and exit void fraction are small. With an abundance of liquid flow, aided by better ability of the wall jets to break through coalescent vapor masses along the surface, there is only limited escalation in surface temperature at CHF.

3.7. Heated Surface Patterns of Arrays

Complex 3D design of the jet impingement module precludes direct optical access to the impingement zones or flow within the confinement region. However, clear local burnout-related patterns were observed along the heating surface after reaching CHF, and these patterns provided valuable insight into the complex inter-

actions among jets when using jet arrays. Similar burnout/fouling patterns were reported by Monde *et al.* [36] for free-surface water jet arrays following CHF. They reported a whitening of the surface away from the jet centers, which they attributed to overheating/burnout in those locations and a consequent fouling caused by film boiling.

Figure 13(a) shows photographs of the heated surface in the present study before and after experiments, with the outlet plenum and the jet plate all scaled in size. With a plan to conduct numerous experimental test cases, it was necessary to retain the integrity of the jet impingement module and to prevent unnecessary leaks between the many layers shown in Fig. 3. Prior to testing any module configuration, the heated surface is thoroughly cleaned with a combination of isopropanol and acetone to eliminate any contaminants or traces of burnout from previous tests. For every module configuration, testing is performed for different jet nozzle velocities, different system saturation pressures, and heat fluxes from zero to CHF. The module is opened afterwards and different burnout patterns are carefully examined. The burnout pattern in Fig. 13(a) is for a 6×6 jet array with $D_n = 0.40$ mm impinging on the Large heated surface. Notice how regions incurring higher surface temperatures are much darker than those directly beneath the jets. Figure 13(b) provides an enlarged image of the same, allowing closer inspection of the different surface regions. The geometrical centers of the jet plate nozzles are marked each with an 'x' for reference. Aside from the localized darkening of higher temperature regions, it is clear that the lighter and darker regions are associated with high fluid shear and low shear, respectively. Notice how the light, high shear regions are present mostly within the impingement zone while dark, low shear regions reside where wall jets emanating from neighboring jets collide and the fluid stagnates. It is clear in Fig. 13(b) that the surface patterns associated with the four central jets are almost perfectly circular and symmetrical around the nozzle centerline, meaning that those jets incur very limited interference from one another. After impingement, the bulk fluid moves mostly in two directions (left and right) towards the outlet plenums. This causes wall jets of the inner impinging jets to push the other outlying jets outwards in the direction of the bulk fluid flow. This behavior is depicted in Fig. 13(a) in which the outer jets appear inclined away from the respective nozzles' geometrical centers and with oval impingement regions, albeit remaining symmetrical with respect to the vertical

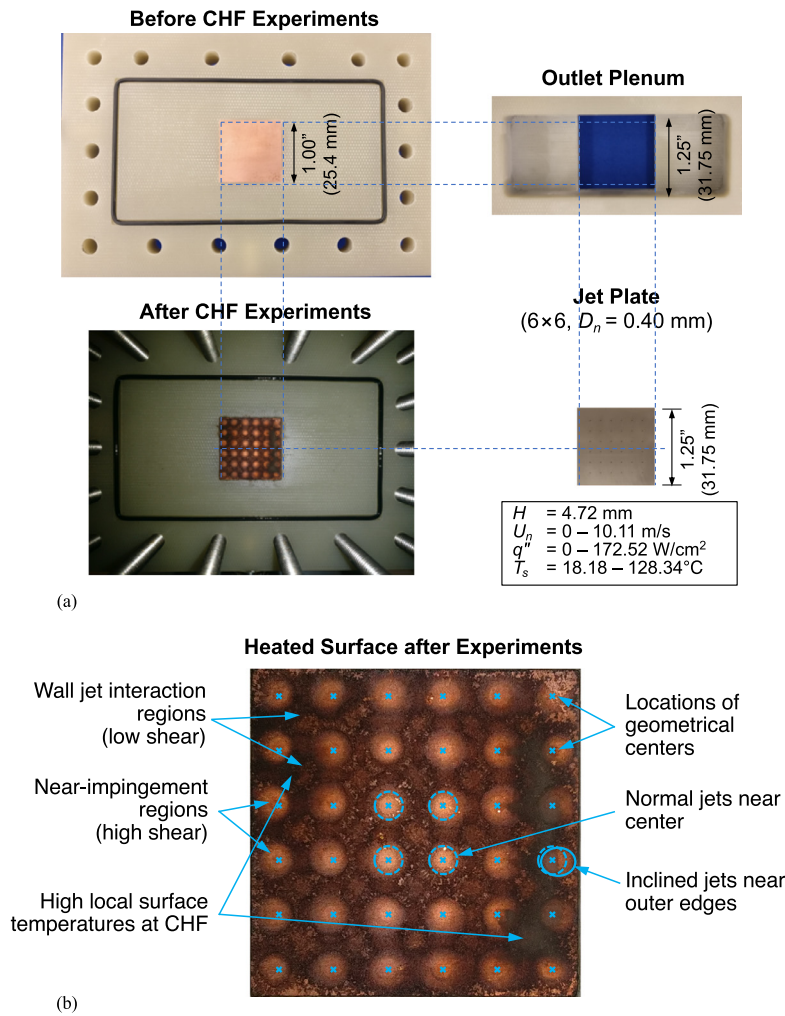


Fig. 13. (a) Photographs of Large surface before and after CHF experiments. (b) Interpretations of key fluid flow and burnout features.

as well as horizontal centerlines of the heated surface. It should be noted that the lighter regions are not entirely due to direct fluid impingement but are the result of fast-moving portions of the wall jets.

Figure 14 shows surface patterns for 3×3 and 6×6 arrays captured following a series of CHF experiments. Indicated below each are detailed values for each set of tests in terms of ranges of jet velocity, heat flux, and corresponding surface temperature, as well as number of steady-state single-phase and nucleate boiling data points, n_{SS} , and number of CHF data points, n_{CHF} , before the module was disassembled and surface pattern photographed.

Comparing the 3×3 array surface patterns for $D_n = 0.40$ to those for $D_n = 0.79$ mm, which correspond to fairly equal jet velocity ranges, shows a much darker surface for the latter, apparently because of higher ranges of both heat flux and surface temperature for the latter. And for the 6×6 array, surface patterns for $D_n = 2.06$ mm are quite faded compared to those for $D_n = 0.79$ mm, which may be attributed to smaller ranges of both heat flux and surface temperature and possibly smaller number of CHF tests for the latter. Another notable observation is the dark spots at jet centers for the 6×6 array with $D_n = 0.79$ mm, which correspond to central low-shear portions of the impingement zones (stagnation zone CHF). Overall, both the 3×3 and 6×6 arrays show distinct lines of demarcation between jet cells, which correspond to collision fronts between wall jets.

4. Development of CHF Correlation

4.1. Correlation Method

A correlation is developed as a predictive tool for CHF for confined round single jets and jet arrays over a fairly broad range of operating conditions. The database used to construct the correlation is comprised of (i) R-134a data collected from experiments conducted in the present study and (ii) previous PU-BTPFL FC-72 database, including those published by Johns and Mudawar for single jets [22] and unpublished jet array data [52]. Combination of these specific data sets is intended to provide a new design tool for fluids commonly used to cool electronic, power and aerospace devices, rather than a universal tool for all fluid types. Table 3 provides a brief summary of the compiled database upon which the correlation is constructed along with ranges of all relevant parameters.

Based on a comprehensive review of prior jet impingement correlations, a complete list of dimensionless parameters is compiled, which is presented in Table 4. One reference is given for each term as an example. These terms correspond to correlations for both a single jet and jet arrays, round and slot jets, circular and rectangular heating surfaces, and free surface, submerged, and confined jet configurations. Correlations are typically a product of some of these terms raised to different powers. For confined round single jets and jet arrays impinging on a square surface, the most com-

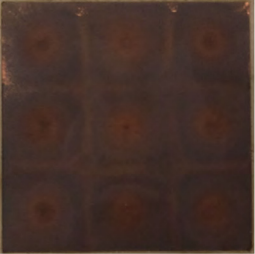
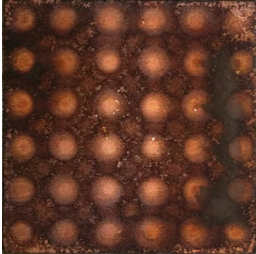
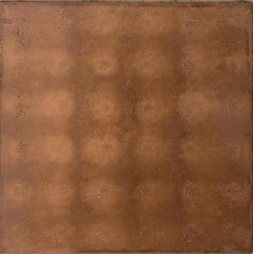
	$D_n = 0.40$ mm	$D_n = 0.79$ mm	$D_n = 2.06$ mm
3 × 3 array			
	$H = 4.72$ mm $U_n = 0 - 9.98$ m/s $q'' = 0 - 113.09$ W/cm ² $T_{s,SS} = 19.86 - 79.62$ °C $n_{SS} = 232$ cases $n_{CHF} = 33$ cases	$H = 4.72$ mm $U_n = 0 - 10.03$ m/s $q'' = 0 - 135.34$ W/cm ² $T_{s,SS} = 20.00 - 92.63$ °C $n_{SS} = 125$ cases $n_{CHF} = 15$ cases	$H = 4.72$ mm $U_n = 0 - 5.02$ m/s $q'' = 0 - 220.86$ W/cm ² $T_{s,SS} = 18.00 - 82.48$ °C $n_{SS} = 198$ cases $n_{CHF} = 16$ cases
6 × 6 array			
	$H = 4.72$ mm $U_n = 0 - 10.11$ m/s $q'' = 0 - 172.52$ W/cm ² $T_{s,SS} = 18.18 - 128.34$ °C $n_{SS} = 351$ cases $n_{CHF} = 31$ cases	$H = 4.72$ mm $U_n = 0 - 9.04$ m/s $q'' = 0 - 232.40$ W/cm ² $T_{s,SS} = 17.96 - 102.63$ °C $n_{SS} = 239$ cases $n_{CHF} = 18$ cases	$H = 4.72$ mm $U_n = 0 - 1.26$ m/s $q'' = 0 - 143.20$ W/cm ² $T_{s,SS} = 18.63 - 98.97$ °C $n_{SS} = 101$ cases $n_{CHF} = 8$ cases

Fig. 14. Post-CHF Large surface patterns for different jet impingement module configurations.

Table 3
Correlation database information with parameters needed to formulate the correlation.

	Present Study	Johns and Mudawar's single jets [22] and jet arrays [52]
Number of datapoints, n	152	168
Fluid	R-134a	FC-72
Number of jets, N	1, 3 × 3, 6 × 6	1, 2 × 2, 3 × 3
Diameter of nozzle, D_n	0.40, 0.79, 2.06 mm	0.40, 0.79, 2.06 mm
Heated area, A_s	25.4 × 25.4 mm ²	12.7 × 12.7, 6.35 × 6.35, 4.23 × 4.23 mm ²
Jet Height, H	4.724 mm	2.03 mm
Jet nozzle velocity, U_n	0.50 - 10.08 m/s	0.125 - 6.0 m/s
Inlet subcooling, $\Delta T_{sub,in}$	1.50 - 13.03 °C	10, 25, 40 °C
Saturation (outlet) pressure, P_{sat}	612,202 - 837,410 Pa(88.79 - 121.46 psia)	124,106 Pa(18 psia)
Critical heat flux, q''_{CHF}	16.88 - 222.84 W/cm ²	20.2 - 254.6 W/cm ²
T_s at CHF	36.45 - 128.20 °C	68.1 - 114 °C

prehensive functional form of the correlation is determined to be

$$\left(\frac{q''_{CHF}}{\rho_g h_{fg} U_n} \right) = fn \left\{ N, \left[\frac{NA_n}{A_s} = \frac{A_n}{A_c} \right], \frac{D_n}{L - D_n}, \frac{H}{D_n}, \left[\frac{\rho_f}{\rho_g} \text{Or} \frac{P_{out}}{P_{crit}} \right], \dots \right\}, \quad (6)$$

where possible heating surface length scales are $L = \{\sqrt{2}L_c, L_c, \sqrt{2}L_h, L_h\}$.

'Statistical inference' techniques [68–70] are used in conjunction with fluid flow and heat transfer physics in the development of this correlation. A multivariate analysis is done using JMP Pro software to examine the influence of each dimensionless parameter on dimensionless CHF, from which the most important parameters are identified. Hypothesis testing is a statistical analysis technique that uses an existing database to assess two mutually exclusive theories about the properties of the data: null and alternative hypotheses [69,70]. Null hypothesis states that there is absolutely

no effect of one parameter on another; and alternative hypothesis is the opposite of null hypothesis, meaning that there is a non-zero effect of an independent parameter on a dependent parameter. The usual practice is to consider the null as default unless the database provides a significantly strong evidence that it can be rejected [69]. The strength of this evidence is specified by the 'significance level', which is a fraction or percentage that signifies the risk of deciding that an effect exists, when it does not. Numerous combinations of dimensionless parameters are investigated so that the non-linear regression in MATLAB software yields coefficients with a t-statistic value of each dimensionless parameter much greater than 1 and a corresponding p-value very close to 0. This means that the corresponding parameter affects CHF and the null hypothesis is invalidated. The t-statistic is defined for each coefficient as the ratio of the regression estimate to the standard error of the coefficient, and is used to infer if a particular term does have significant influence

Table 4
Dimensionless terms used in past jet impingement CHF correlations.

Description	Definition/Formulation
Dimensionless critical heat flux, q''_{CHF}	$\frac{q''_{CHF}}{\rho_g h_{fg} U_n}$ [24], $\frac{q''_{CHF}}{G h_{fg}}$ [35], $\frac{q''_{CHF}}{q''_{CHF,pool}}$ [45]
Density ratio, $\frac{\rho_l}{\rho_g}$	$\frac{\rho_l}{\rho_g}$ [24], $1 + \frac{\rho_g}{\rho_f}$ [32], $C_1 + C_2 \frac{\rho_l}{\rho_g}$ [37], $\ln(\frac{\rho_l}{\rho_g})$ [37]
Weber number, We (We^{-1} is typically shown in correlations and is given here)	$\frac{\sigma}{\rho_f U_n^2 D_n}$ [24], $\frac{\sigma}{\rho_f U_n^2 L}$ [29], $\frac{2\sigma}{\rho_f U_n^2 L_{ch}}$ [36], $\frac{2\sigma}{\rho_f U_n^2 (D_n - D_n)}$ [33], $\frac{\sigma}{\rho_f U_n^2 2L}$ [38], $\frac{\sigma}{\rho_f U_n^2 (L - W_n)}$ [39], $\frac{2\sigma}{\rho_f U_n^2 (L - D_n)}$ [41], $\frac{\sigma(\rho_l - \rho_g)}{\rho_f^2 U_n^2 (D_n - D_n)}$ [74]
Subcooling effectiveness, ε_{sub}	$1 + \varepsilon_{sub}$ [24], where $\varepsilon_{sub} = fn(\frac{\rho_l}{\rho_g}, Ja^*)$ [24]
Modified Jakob number, Ja^*	$\frac{c_{p,f}(T_{sat} - T_{in})}{h_{fg}}$ [24], $1 + \frac{c_{p,f} \Delta T_{sub,in}}{h_{fg}}$ [39], $1 + C_{sub} \frac{\rho_l c_{p,f} \Delta T_{sub,in}}{\rho_g h_{fg}}$ [39]
Dimensionless geometrical parameters	$1 + \frac{D_n}{D_n}$ [33], $1 + C(\frac{L_{sub}}{D_n})^2$ [36], $\frac{D_n}{D_n}$ [37], $1 + \frac{L}{D_n}$ [41], $\frac{L}{D_n}$ [41], $\frac{D_n}{L_n - D_n}$ [22], $\frac{D_n}{\lambda_c}$ [45], $\frac{D_n}{\lambda_c}$ [34], $\frac{W_n}{L - W_n}$ [39], $\frac{D_n - D_n}{\lambda_c}$ [46], Ar [43]
Number of jets, N	N [43], $1 + C_1 N^{C_2}$ [44]
Reynolds number, Re	$\frac{\rho_f U_n D_n}{\mu_f}$ [45]
Archimedes number, Ar	$\frac{\rho_l g(\rho_l - \rho_g) D_n^3}{\mu_f^2}$ [45]
Froude number, Fr	$Fr_{\lambda,c} = \frac{U_n}{\sqrt{g \lambda_c}}$ [46]
Other parameters	$\frac{k_f}{c_{p,f} G D_n}$ [48]

on the correlation model, meaning that the alternate hypothesis is valid. The p-value (probability value) is the largest probability that any other experiment will yield the same value as determined from the current database, if the null hypothesis is true and the chosen model is correct. A key rule of thumb is to reject the null hypothesis when the p-value is less than or equal to 0.05, which is equivalent to a 5% significance level for a parameter [68,71]. This would also help identify correlation forms in which two or more terms are interrelated or have a similar effect on CHF, and where one can be neglected. The result of this analysis was the reduction of the functional form in Eq. (6) to

$$\left(\frac{q''_{CHF}}{\rho_g h_{fg} U_n} \right) = fn \left\{ N, \frac{NA_n}{A_s}, \frac{\rho_f}{\rho_g}, \frac{\sigma}{\rho_f U_n^2 (\sqrt{2}L_c - D_n)}, \frac{c_{p,f} \Delta T_{sub,in}}{h_{fg}} \right\}. \tag{7}$$

Performing a non-linear regression on the entire functional form in Eq. (7) can lead to non-physical coefficients because the fitting is done by numerical means. To alleviate this concern, exponents of the density ratio and two modified Jakob number terms are fixed at 2/3, 2/3, and 1/3, respectively, based on analysis done by Mudawar and Wadsworth [39] for a single two-dimensional confined jet and adopted in other confined jet correlations [21,22,43].

$$\left(\frac{q''_{CHF}}{\rho_g h_{fg} U_n} \right) = C_1 \left(\frac{\sigma}{\rho_f U_n^2 (\sqrt{2}L_c - D_n)} \right)^{C_2} \left(\frac{\rho_f}{\rho_g} \right)^{2/3} \left(\frac{NA_n}{A_s} \right)^{C_3} \dots \left(1 + C_4 \frac{\rho_f c_{p,f} \Delta T_{sub,in}}{\rho_g h_{fg}} \right)^{2/3} \left(1 + \frac{c_{p,f} \Delta T_{sub,in}}{h_{fg}} \right)^{1/3} N^{C_5}. \tag{8}$$

The non-linear regression is performed using a 'bisquare robust weighting function' with a tuning constant of 4.685 [72], and the entire correlation model's 'F-statistic' is made sure to be much greater than 1 and the corresponding p-value very close to zero. The F-statistic is used to test the overall statistical significance of the correlation model, whether it would be the best fit for the database [69]. In other words, the F-statistic indicates whether a chosen correlation model better predicts CHF (dependent parameter) than a model that contains no independent parameters (i.e., with all regression coefficients equal to zero; a zero model). It is noted that a t-statistic assesses a particular dimensionless term whereas the F-statistic assesses the entire correlation model. It can be seen in Table 3 that jet height is different between the R-134a and FC-72 databases, yet it does not appear in Eq. (8) because,

as mentioned earlier, of its weak effect on CHF for moderate jet heights [22,38,39,67]. Geometrical effects of the jet on CHF are accounted for in the ratio of the total area of all jet nozzles to the heated surface area, $Ar = NA_n/A_s$, which is the same as the ratio of a single jet area to the jet cell area, A_n/A_c . This parameter considers the important effect of heated surface size, which governs where potential dryout would occur. Dryout is typically observed in single jet CHF experiments at the edges of the heated surface [22,27,73] and in the wall jet interaction regions for jet arrays. For a particular set of operating conditions, CHF is higher for higher area ratios because of shorter wall jets [22,52]. For a round jet impinging on a square heated surface, CHF is expected at the four diagonal corners, meaning that the characteristic length of the heated surface with respect to the nozzle diameter is the diagonal length, $L_{char} = \sqrt{2}L_c$. Researchers have defined this to be distance from the center of the jet to the farthest point within the unit jet cell for complicated geometries [36]. An alternative half-diagonal length of $L_{char} = \sqrt{2}L_c/2$ was used by Copeland [43] for similar geometries. Jet interaction effects in jet array configurations are also accounted for by the number of jets, N , where $N = 1$ for a single jet, which is free from jet interactions. Weber number accounts for both the fluid properties and characteristic length scale effects and is a measure of liquid-vapor interfacial instabilities. The density ratio term accounts for both fluid type and saturation pressure. Finally, the modified Jakob number terms tackle the subcooling effects [39].

4.2. New Correlation and its Performance

The resulting correlation is

$$q''_{CHF} = \left(\frac{q''_{CHF}}{\rho_g h_{fg} U_n} \right) = 0.270 \left(\frac{\sigma}{\rho_f U_n^2 (\sqrt{2}L_c - D_n)} \right)^{0.277} \left(\frac{\rho_f}{\rho_g} \right)^{2/3} \left(\frac{NA_n}{A_s} \right)^{0.259} \dots \left(1 + 0.034 \frac{\rho_f c_{p,f} \Delta T_{sub,i}}{\rho_g h_{fg}} \right)^{2/3} \left(1 + \frac{c_{p,f} \Delta T_{sub,i}}{h_{fg}} \right)^{1/3} N^{-0.109} \tag{9}$$

which has an overall Mean Absolute Error (MAE) of 16.66 %, Root Mean Square Error (RMSE) of 22.02 %, and an R-squared value of 0.991, where

$$MAE (\%) = \frac{1}{n} \sum \left[\frac{|q''_{CHF,pred} - q''_{CHF,exp}|}{q''_{CHF,exp}} \right] \times 100 \tag{10}$$

and

$$RMSE (\%) = \sqrt{\frac{1}{n} \sum \left[\frac{q''_{CHF,pred} - q''_{CHF,exp}}{q''_{CHF,exp}} \right]^2} \times 100. \tag{11}$$

Table 5
Important statistical information for the new correlation.

Coefficients	Estimate	Std. Error	t-Statistic	p-Value
C_1	0.2702	0.0097	27.935	3.01×10^{-87}
C_2	0.2766	0.0018	149.84	7.31×10^{-295}
C_3	0.2589	0.0068	37.824	3.73×10^{-119}
C_4	0.0338	0.0014	24.827	3.86×10^{-76}
C_5	-0.1091	0.0089	-12.294	1.22×10^{-28}
F-statistic (versus zero model)	9.48×10^3			
Overall p-value of model	0			
Mean Absolute Error, MAE	16.66%			
Root Mean Square Error, RMSE	22.02%			
R-squared value	0.991			
$\pm 30\%$ prediction inliers, θ	84.06%			
$\pm 50\%$ prediction inliers, ξ	97.50%			

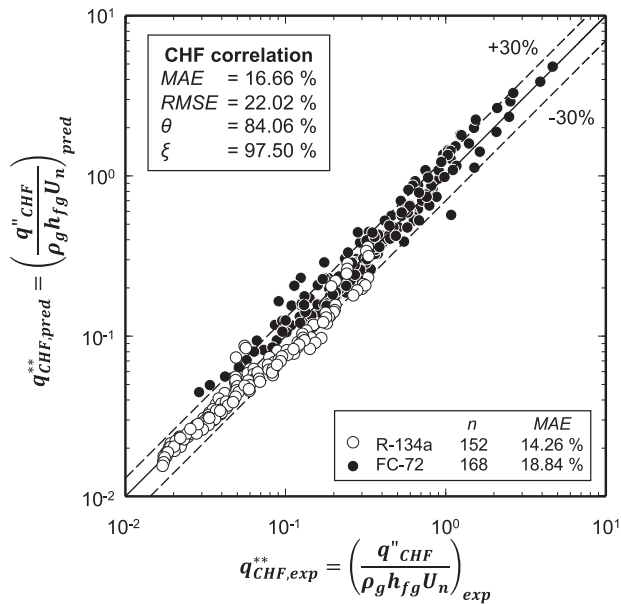


Fig. 15. Comparison of predictions of the new jet impingement CHF correlation with the compiled experimental database.

Table 5 provides additional statistical information related to the final correlation regression. It clearly shows that the magnitudes of all t-statistic and F-statistic values are much greater than unity and corresponding p-values much less than 0.05. All thermophysical properties are evaluated at the outlet plenum (saturation) pressure.

Of all the correlation forms tested, Eq. (9) yielded the lowest MAE. With an almost equal number of datapoints between the two fluids and a decent scatter of datapoints over the entire ranges of relevant parameters, a separate prediction performance test for smaller blocks of the database is unwarranted. It is interesting to note that the new correlation in Eq. (9) coincidentally ended up being somewhat similar to that of Johns and Mudawar [22], which was proposed for a single confined round jet of FC-72 impinging onto a square surface. Their correlation was a simple adaptation of Mudawar and Wadsworth's [39] single slot jet correlation, but with different empirical constants. The main improvements here seem to be (i) usage of a characteristic heated length scale instead of the heated surface side length, (ii) geometrical effects given by the area ratio instead of a diameter based ratio, $D_n/(L_h - D_n)$, and (iii) inclusion of number of jets. Eq. (9) also highlights CHF degradation due to wall jet interactions in jet arrays ($q''_{CHF} \sim N^{-0.109}$).

Figure 15 shows the performance of the new correlation with the compiled experimental database upon which it is constructed. Reference lines are indicated for a perfect prediction, and $\pm 30\%$ er-

rors using a solid and dashed lines, respectively. Datapoints for the two comprised fluids are denoted using different plot markers. The performance of the correlation in predicting the experimental data is assessed by different statistical parameters: MAE, RMSE and inliers θ , and ξ . MAE treats the absolute error from each datapoint equally, whereas RMSE gives a higher weight to outliers. RMSE is slightly higher than MAE but indicates that the correlation performs quite effectively for most of the database, and the MAE of 16.66% appears to be the result of deviations caused by very few datapoints. Figure 15 shows 84.06% and 97.50% of datapoints fall within $\pm 30\%$ (θ value) and $\pm 50\%$ (ξ value) of the measured values, respectively. This further substantiates that the prediction performance is good for the majority of the database. It is also evident that both fluids perform evenly over all three orders of magnitude of dimensionless CHF. Between the two, R-134a shows smaller scatter than FC-72, which is evidenced by the single fluid MAE values of 14.26% for the former and 18.84% for the latter.

5. Conclusions

The present study involved experimental investigation of parameters influencing CHF for confined round single jets and jet arrays impinging normally onto square heated surfaces. The experiments were performed using R-134a, a fluid widely used for thermal management of electronic and power devices especially in aerospace applications, for which jet impingement information is quite sparse. A comprehensive R-134a CHF database was acquired that considers the effects of various geometrical parameters and operating conditions. Close inspection of the heating surface following CHF tests showed localized burnout patterns which provided significant insight into both the flow characteristics within the confinement region and the spatial distribution of surface temperature resulting from jet interactions. Key findings from the study are as follows:

- (1) Jet velocity has a far stronger influence on CHF than mass flow rate. CHF increases with increasing jet velocity, with stronger dependence realized at lower velocities.
- (2) CHF increases with increasing nozzle diameter for a fixed jet velocity, and slightly decreases with increasing nozzle diameter for a fixed mass flow rate. Augmentation of CHF with larger diameters is greater for slower jets.
- (3) Jet arrays yield higher CHF than a single jet for a fixed jet velocity, but lower CHF for a fixed mass flow rate. Increasing the number of jets for a fixed heated surface area has similar effects, with greater CHF augmentation achieved at lower velocities. For a fixed flow rate and a comparatively high area ratio, CHF increases by using fewer jets, albeit at the expense of greater pressure drop. This shows efforts to improve CHF must always be weighed against the drawback of increased pumping power.
- (4) Increasing saturation pressure slightly increases CHF for a fixed inlet fluid temperature. This augmentation is more pronounced at higher velocities for jet arrays.
- (5) Negative exit qualities indicate most high mass flow rate cases encountered fully subcooled CHF, which is comprised of the fluid exiting the module in pure liquid state following partial localized dryout within the confinement region. On the other hand, exit qualities at CHF for lower flow rates are typically high, indicative of saturated CHF conditions.
- (6) Two types of CHF occurrence were observed: sharp heating block temperature escalation at lower flow rates, and a mild prolonged temperature increase at higher flow rates. Underlying mechanisms for the two transient types have been propounded.
- (7) A new CHF design correlation was constructed based on a consolidated database comprised of the present R-134a data and

previous FC-72 data. A thorough review of literature identified numerous correlations, their formulation rationale, and key dimensionless terms used. Statistical inference techniques were used in conjunction with a new understanding of the fluid flow and heat transfer physics to formulate a new correlation form. The new correlation shows good prediction accuracy, evidenced by 16.66% mean absolute error, 22.02% root mean square error, and 0.991 R-squared value for both fluids and over broad ranges of geometrical parameters and operating conditions. Additionally, 84.06% and 97.50% of the predicted CHF values are within $\pm 30\%$ and $\pm 50\%$, respectively, of corresponding experimental values.

Declaration of Competing Interest

The authors declare that they have no known competing financial interests or personal relationships that could have appeared to influence the work reported in this paper.

Acknowledgement

The authors are appreciative for the support of the Center for Integrated Thermal Management for Aerospace Vehicles (CITMAV) under grant No. 40001302.

References

- [1] I. Mudawar, Assessment of high-heat-flux thermal management schemes, *IEEE Trans. Compon. Packag. Technol.* 24 (2) (2001) 122–141, doi:10.1109/6144.926375.
- [2] J. Lee, I. Mudawar, Critical heat flux for subcooled flow boiling in micro-channel heat sinks, *Int. J. Heat Mass Transfer* 52 (13–14) (2009) 3341–3352, doi:10.1016/j.ijheatmasstransfer.2008.12.019.
- [3] T.J. LaClair, I. Mudawar, Thermal transients in a capillary evaporator prior to the initiation of boiling, *Int. J. Heat Mass Transfer* 43 (21) (2000) 3937–3952, doi:10.1016/S0017-9310(00)00042-9.
- [4] I. Mudawar, T.M. Anderson, Parametric investigation into the effects of pressure, subcooling, surface augmentation and choice of coolant on pool boiling in the design of cooling systems for high-power-density electronic chips, *J. Electron. Packag.* 112 (4) (1990) 375–382, doi:10.1115/1.2904392.
- [5] I. Mudawar, T.M. Anderson, Optimization of enhanced surfaces for high flux chip cooling by pool boiling, *J. Electron. Packag.* 115 (1) (1993) 89–100, doi:10.1115/1.2909306.
- [6] G. Liang, I. Mudawar, Pool boiling critical heat flux (CHF) – Part 1: Review of mechanisms, models, and correlations, *Int. J. Heat Mass Transfer* 117 (2018) 1352–1367, doi:10.1016/j.ijheatmasstransfer.2017.09.134.
- [7] J.A. Shmerler, I. Mudawar, Local evaporative heat transfer coefficient in turbulent free-falling liquid films, *Int. J. Heat Mass Transfer* 31 (4) (1988) 731–742, doi:10.1016/0017-9310(88)90131-7.
- [8] T.H. Lyu, I. Mudawar, Statistical investigation of the relationship between interfacial waviness and sensible heat transfer to a falling liquid film, *Int. J. Heat Mass Transfer* 34 (6) (1991) 1451–1464, doi:10.1016/0017-9310(91)90288-P.
- [9] D.E. Maddox, I. Mudawar, Single- and two-phase convective heat transfer from smooth and enhanced microelectronic heat sources in a rectangular channel, *J. Heat Transfer* 111 (4) (1989) 1045–1052, doi:10.1115/1.3250766.
- [10] C.O. Gersey, I. Mudawar, Effects of heater length and orientation on the trigger mechanism for near-saturated flow boiling critical heat flux—I. Photographic study and statistical characterization of the near-wall interfacial features, *Int. J. Heat Mass Transfer* 38 (4) (1995) 629–641, doi:10.1016/0017-9310(94)00193-Y.
- [11] T.C. Willingham, I. Mudawar, Forced-convection boiling and critical heat flux from a linear array of discrete heat sources, *Int. J. Heat Mass Transfer* 35 (11) (1992) 2879–2890, doi:10.1016/0017-9310(92)90308-F.
- [12] S. Mukherjee, I. Mudawar, Smart, low-cost, pumpless loop for micro-channel electronic cooling using flat and enhanced surfaces, in: 8th Intersoc, in: *Conf. Therm. Thermomech. Phenom. Electron. Syst.*, IEEE, San Diego, CA, USA, 2002, pp. 360–370, doi:10.1109/ITHERM.2002.1012479.
- [13] S.M. Kim, I. Mudawar, Universal approach to predicting saturated flow boiling heat transfer in mini/micro-channels – Part I. Dryout incipience quality, *Int. J. Heat Mass Transfer* 64 (2013) 1226–1238, doi:10.1016/j.ijheatmasstransfer.2013.04.016.
- [14] S.M. Kim, I. Mudawar, Review of databases and predictive methods for pressure drop in adiabatic, condensing and boiling mini/micro-channel flows, *Int. J. Heat Mass Transfer* 77 (2014) 74–97, doi:10.1016/j.ijheatmasstransfer.2014.04.035.
- [15] W.P. Klinzing, J.C. Rozzi, I. Mudawar, Film and transition boiling correlations for quenching of hot surfaces with water sprays, *J. Heat Treat.* 9 (2) (1992) 91–103, doi:10.1007/BF02833145.
- [16] D.C. Wadsworth, I. Mudawar, Enhancement of single-phase heat transfer and critical heat flux from an ultra-high-flux simulated microelectronic heat source to a rectangular impinging jet of dielectric liquid, *J. Heat Transfer* 114 (3) (1992) 764–768, doi:10.1115/1.2911348.
- [17] I. Mudawar, Recent advances in high-flux, two-phase thermal management, *J. Therm. Sci. Eng. Appl.* 5 (2) (2013) 021012, doi:10.1115/1.4023599.
- [18] R.A. Buchanan, T.A. Shedd, Extensive parametric study of heat transfer to arrays of oblique impinging jets with phase change, *J. Heat Transfer* 135 (11) (2013), doi:10.1115/1.4024625.
- [19] R. Viskanta, Heat transfer to impinging isothermal gas and flame jets, *Exp. Therm. Fluid Sci.* 6 (2) (1993) 111–134, doi:10.1016/0894-1777(93)90022-B.
- [20] Y. Katto, M. Kunihiro, Study of the mechanism of burn-out in boiling system of high burn-out heat flux, *Bull. JSME* 16 (99) (1973) 1357–1366, doi:10.1299/jsme1958.16.1357.
- [21] M.T. Meyer, I. Mudawar, C.E. Boyack, C.A. Hale, Single-phase and two-phase cooling with an array of rectangular jets, *Int. J. Heat Mass Transfer* 49 (1–2) (2006) 17–29, doi:10.1016/j.ijheatmasstransfer.2005.07.039.
- [22] M.E. Johns, I. Mudawar, An ultra-high power two-phase jet-impingement avionic clamshell module, *J. Electron. Packag.* 118 (4) (1996) 264–270, doi:10.1115/1.2792162.
- [23] R. Cardenas, V. Narayanan, Heat transfer characteristics of submerged jet impingement boiling of saturated FC-72, *Int. J. Heat Mass Transfer* 55 (15–16) (2012) 4217–4231, doi:10.1016/j.ijheatmasstransfer.2012.03.063.
- [24] M. Monde, Y. Katto, Burnout in a high heat-flux boiling system with an impinging jet, *Int. J. Heat Mass Transfer* 21 (3) (1978) 295–305, doi:10.1016/0017-9310(78)90122-9.
- [25] Y. Katto, M. Shimizu, Upper limit of CHF in the saturated forced convection boiling on a heated disk with a small impinging jet, *J. Heat Transfer* 101 (2) (1979) 265–269, doi:10.1115/1.3450958.
- [26] M. Monde, Critical heat flux in saturated forced convection boiling on a heated disk with an impinging jet, *J. Heat Transfer* 109 (4) (1987) 991–996, doi:10.1115/1.3248215.
- [27] K.A. Estes, I. Mudawar, Comparison of two-phase electronic cooling using free jets and sprays, *J. Electron. Packag.* 117 (4) (1995) 323–332, doi:10.1115/1.2792112.
- [28] R.W. Murphy, A.E. Bergles, *Subcooled Flow Boiling of Fluorocarbons*, Report No. DSR 71903-72, Massachusetts Institute of Technology, Cambridge, MA, USA, 1971.
- [29] Y. Katto, K. Ishii, Burnout in a high heat flux boiling system with a forced supply of liquid through a plane jet, *Trans. Jpn. Soc. Mech. Eng.* 44 (384) (1978) 2817–2823, doi:10.1299/kikai1938.44.2817.
- [30] Y. Katto, C. Kurata, Critical heat flux of saturated convective boiling on uniformly heated plates in a parallel flow, *Int. J. Multiphase Flow* 6 (6) (1980) 575–582, doi:10.1016/0301-9322(80)90052-X.
- [31] M. Monde, Burnout heat flux in saturated forced convection boiling with an impinging jet, *Heat Transfer - Japanese Res.* 9 (1980) 31–41.
- [32] Y. Haramura, Y. Katto, A new hydrodynamic model of critical heat flux, applicable widely to both pool and forced convection boiling on submerged bodies in saturated liquids, *Int. J. Heat Mass Transfer* 26 (3) (1983) 389–399, doi:10.1016/0017-9310(83)90043-1.
- [33] M. Monde, Critical heat flux in saturated forced convective boiling on a heated disk with an impinging jet, *Wärme- Und Stoffübertragung* 19 (1985) 205–209, doi:10.1007/BF01403758.
- [34] M. Monde, Y. Okuma, Critical heat flux in saturated forced convective boiling on a heated disk with an impinging jet—CHF in L-regime, *Int. J. Heat Mass Transfer* 28 (3) (1985) 547–552, doi:10.1016/0017-9310(85)90177-2.
- [35] Y. Katto, S. Yokoya, Critical heat flux on a disk heater cooled by a circular jet of saturated liquid impinging at the center, *Int. J. Heat Mass Transfer* 31 (2) (1988) 219–227, doi:10.1016/0017-9310(88)90003-8.
- [36] M. Monde, H. Kusuda, H. Uehara, Burnout heat flux in saturated forced convection boiling with two or more impinging jets, *Heat Transfer - Japanese Res.* 9 (3) (1980) 18–31.
- [37] A. Sharan, J.H. Lienhard, On predicting burnout in the jet-disk configuration, *J. Heat Transfer* 107 (2) (1985) 398–401, doi:10.1115/1.3247428.
- [38] T. Nonn, Z. Dagan, L.M. Jiji, *Boiling jet impingement cooling of simulated microelectronic heat sources*, ASME Paper No. 88-WA/EEP-3, 1988.
- [39] I. Mudawar, D.C. Wadsworth, Critical heat flux from a simulated chip to a confined rectangular impinging jet of dielectric liquid, *Int. J. Heat Mass Transfer* 34 (6) (1991) 1465–1479, doi:10.1016/0017-9310(91)90289-Q.
- [40] W.R. McGillis, V.P. Carey, *Immersion cooling of an array of heat dissipating elements. An assessment of different flow boiling methodologies*, *Cryog. Immersion Cool. Opt. Electron. Equip.* (1990) 37–44.
- [41] M. Monde, K. Kitajima, T. Inoue, Y. Mitsutake, Critical heat flux in a forced convective subcooled boiling with an impinging jet, in: *Int. Heat Transfer Conf.*, Digital Library, Begell House Inc., 1994, pp. 515–520, doi:10.1615/IHTC10.1380.
- [42] D. Copeland, Single-phase and boiling cooling of small pin fin arrays by multiple slot nozzle suction and impingement, *IEEE Trans. Compon. Packag. Manuf. Technol. Part A* 18 (3) (1995) 510–516, doi:10.1109/95.465145.
- [43] D. Copeland, Single-phase and boiling cooling of small pin fin arrays by multiple nozzle jet impingement, *J. Electron. Packag.* 118 (1) (1996) 21–26, doi:10.1115/1.2792122.
- [44] T. Cong, R. Chen, G. Su, S. Qiu, W. Tian, Analysis of CHF in saturated forced convective boiling on a heated surface with impinging jets using artificial neural network and genetic algorithm, *Nucl. Eng. Des.* 241 (9) (2011) 3945–3951, doi:10.1016/j.nucengdes.2011.07.029.

- [45] R. Cardenas, V. Narayanan, A generalized critical heat flux correlation for submerged and free surface jet impingement boiling, *J. Heat Transfer* 136 (9) (2014) 1–9, doi:10.1115/1.4027552.
- [46] W. Grassi, D. Testi, A new hydrodynamic approach for jet impingement boiling CHF, *Int. Commun. Heat Mass Transfer* 104 (2019) 83–88, doi:10.1016/j.icheatmasstransfer.2019.02.014.
- [47] Y.Y. Li, Y.J. Chen, Z.H. Liu, Correlations for boiling heat transfer characteristics of high-velocity circular jet impingement on the nano-characteristic stagnation zone, *Int. J. Heat Mass Transfer* 72 (2014) 177–185, doi:10.1016/j.ijheatmasstransfer.2014.01.008.
- [48] Y.Y. Li, Z.H. Liu, Theoretical research of critical heat flux in subcooled impingement boiling on the stagnation zone, *Int. J. Heat Mass Transfer* 55 (25–26) (2012) 7544–7551, doi:10.1016/j.ijheatmasstransfer.2012.07.043.
- [49] Y.H. Qiu, Z.H. Liu, Critical heat flux in saturated and subcooled boiling for R-113 jet impingement on the stagnation zone, *Appl. Therm. Eng.* 25 (14–15) (2005) 2367–2378, doi:10.1016/j.applthermaleng.2004.12.004.
- [50] Z.H. Liu, T.F. Tong, Y.H. Qiu, Critical heat flux of steady boiling for subcooled water jet impingement on the flat stagnation zone, *J. Heat Transfer* 126 (2) (2004) 179–183, doi:10.1115/1.1668054.
- [51] Z.H. Liu, Q.Z. Zhu, Prediction of critical heat flux for convective boiling of saturated water jet impinging on the stagnation zone, *J. Heat Transfer* 124 (6) (2002) 1125–1130, doi:10.1115/1.1518497.
- [52] M.E. Johns, Application of jet impingement boiling in an ultra-high power avionic clamshell module, M.S. Thesis, Purdue University, West Lafayette, IN, USA, 1994.
- [53] D.C. Wadsworth, I. Mudawar, Cooling of a multichip electronic module by means of confined two-dimensional jets of dielectric liquid, *J. Heat Transfer* 112 (4) (1990) 891–898, doi:10.1115/1.2910496.
- [54] G.W. Burns, M.G. Scroger, The calibration of thermocouples and thermocouple materials, *Natl. Inst. Stand. Technol.* 250 (35) (1989).
- [55] E.W. Lemmon, M.L. Huber, M.O. McLinden, Reference Fluid Thermodynamic and Transport Properties - REFPROP, NIST, Gaithersburg, MD, 2007.
- [56] J.G. Collier, J.R. Thome, Convective boiling and condensation, 3rd ed., Clarendon Press, Oxford, 1994.
- [57] C.F. Ma, A.E. Bergles, Jet impingement nucleate boiling, *Int. J. Heat Mass Transfer* 29 (8) (1986) 1095–1101, doi:10.1016/0017-9310(86)90140-7.
- [58] D.T. Vader, G.M. Chrysler, R.C. Chu, R.E. Simons, Experimental investigation of subcooled liquid nitrogen impingement cooling of a silicon chip, *IEEE Trans. Compon. Packag. Manuf. Technol. Part A* 18 (4) (1995) 788–794, doi:10.1109/95.477465.
- [59] L. Qiu, S. Dubey, F.H. Choo, F. Duan, Recent developments of jet impingement nucleate boiling, *Int. J. Heat Mass Transfer* 89 (2015) 42–58, doi:10.1016/j.ijheatmasstransfer.2015.05.025.
- [60] M.K. Sung, I. Mudawar, Correlation of critical heat flux in hybrid jet impingement/micro-channel cooling scheme, *Int. J. Heat Mass Transfer* 49 (15–16) (2006) 2663–2672, doi:10.1016/j.ijheatmasstransfer.2006.01.008.
- [61] D. Copeland, Single-phase and boiling cooling of a small heat source by multiple nozzle jet impingement, *Int. J. Microelectron. Packag.* 1 (1998) 105–113.
- [62] Y. Zhang, W. Chen, Boiling heat transfer of a brass beads-packed porous layer subjected to submerged jet impingement, *Heat Transfer Res* 50 (15) (2019) 1457–1476, doi:10.1615/HeatTransRes.2019027922.
- [63] E.A. Browne, M.K. Jensen, Y. Peles, Microjet array flow boiling with R134a and the effect of dissolved nitrogen, *Int. J. Heat Mass Transfer* 55 (4) (2012) 825–833, doi:10.1016/j.ijheatmasstransfer.2011.10.025.
- [64] C.H. Shin, K.M. Kim, S.H. Lim, H.H. Cho, Influences of nozzle-plate spacing on boiling heat transfer of confined planar dielectric liquid impinging jet, *Int. J. Heat Mass Transfer* 52 (23–24) (2009) 5293–5301, doi:10.1016/j.ijheatmasstransfer.2009.08.002.
- [65] W. Nakayama, M. Behnia, H. Mishima, Impinging jet boiling of a fluorinert liquid on a foil heater array, *J. Electron. Packag.* 122 (2) (2000) 132–137, doi:10.1115/1.483145.
- [66] S. Lee, V.S. Devahdhanush, I. Mudawar, Experimental and analytical investigation of flow loop induced instabilities in micro-channel heat sinks, *Int. J. Heat Mass Transfer* 140 (2019) 303–330, doi:10.1016/j.ijheatmasstransfer.2019.05.077.
- [67] P. Zhang, G.H. Xu, X. Fu, C.R. Li, Confined jet impingement of liquid nitrogen onto different heat transfer surfaces, *Cryogenics* 51 (6) (2011) 300–308, doi:10.1016/j.cryogenics.2010.06.018.
- [68] H.J. Seltman, Experimental Design and Analysis, Department of Statistics, Carnegie Mellon University, 2018 Book only available online at <http://www.stat.cmu.edu/~hseltman/309/Book/Book.pdf>.
- [69] J. Frost, Hypothesis Testing: An Intuitive Guide for Making Data Driven Decisions, 1st ed., 2020 Book only available online at <http://www.statisticsbyjim.com>.
- [70] J. Frost, Regression Analysis: An Intuitive Guide, 1st ed., 2019 Book only available online at <http://www.statisticsbyjim.com>.
- [71] R.B. Darlington, A.F. Hayes, Regression Analysis and Linear Models: Concepts, Application and Implementation, The Guilford Press, New York, NY, 2017.
- [72] P.W. Holland, R.E. Welsch, Robust regression using iteratively reweighted least-squares, *Communications in Statistics - Theory and Methods* 6 (9) (1977) 813–827, doi:10.1080/03610927708827533.
- [73] D.W. Zhou, C.F. Ma, Local jet impingement boiling heat transfer with R113, *Heat Mass Transfer* 40 (6–7) (2004) 539–549, doi:10.1007/s00231-003-0463-7.
- [74] M.R. Pais, L.C. Chow, E.T. Mahefkey, Multiple jet impingement cooling, *J. Thermophys. Heat Transfer* 7 (3) (1993) 435–440, doi:10.2514/3.437.